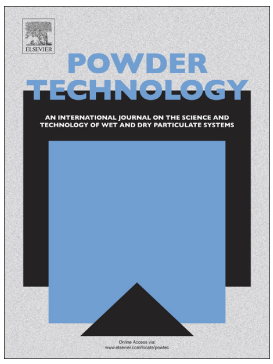

Particle scale modeling of heat transfer in granular flows in a double screw reactor

Fenglei Qi, Mark Mba Wright

PII: S0032-5910(18)30349-8
DOI: doi:10.1016/j.powtec.2018.04.068
Reference: PTEC 13369

To appear in: *Powder Technology*

Received date: 1 September 2017
Revised date: 14 February 2018
Accepted date: 23 April 2018

Please cite this article as: Fenglei Qi, Mark Mba Wright , Particle scale modeling of heat transfer in granular flows in a double screw reactor. The address for the corresponding author was captured as affiliation for all authors. Please check if appropriate. Ptec(2018), doi:10.1016/j.powtec.2018.04.068

Particle scale modeling of heat transfer in granular flows in a double screw reactor

Fenglei Qi[a,*], Mark Mba Wright[b,*]

[a] *Faculty of Science, Technology and Communication, University of Luxembourg, Campus Kirchberg, 6 rue Coudenhove-Kalergi L-1359, Luxembourg*
[b] *Department of Mechanical Engineering, Iowa State University, Ames, Iowa, 50010 USA*

Abstract

Heat transfer in granular flows plays an important role in particulate material processing such as food production, pharmaceuticals and biorenewable energy production. Better understanding of the thermodynamics in granular flows is essential for equipment design and product quality control. In this research, a particle-scale heat transfer model was developed within the frame of traditional Discrete Element Method (DEM), which considers both conductive heat transfer and radiative heat transfer among particles. A particle-wall heat transfer model was also proposed for resolving particle-wall conductive and radiative heat transfer. The developed thermal DEM model was validated by modeling heat transfer in packed beds and comparing simulation predictions with experimental measurements. The thermal DEM model was successfully applied to the simulation of heat transfer in binary component granular flows in a double screw reactor designed for biomass fast pyrolysis to gain better understanding of the heat transfer in the system. The existence of both spatial and temporal temperature oscillations is observed in the double screw reactor. The effects of the operating conditions on the average temperature profile, biomass particle temperature probability distribution, heat flux and heat transfer coefficient are analyzed. Results indicate that the particle-fluid-particle conductive heat transfer pathways are the dominant contributors to the total heat flux, which accounts for approximately 70%-80% in the total heat flux. Radiative heat transfer contributes 14%-26% to the total heat flux and the con-

ductive heat transfer through contact surface takes only 1%-5% in the total heat flux. The total heat transfer coefficient in the double screw reactor is also reported, which varies from 70 to 110 W/(m$^2 \cdot$ K) depending on the operating conditions.

Keywords:

Biomass granular flow; Double screw reactor; Heat transfer coefficient; Radiation; Thermal DEM

1. Introduction

Heat transfer in dense particulate flows has seen a lot of applications in fluidized bed reactors [1, 2, 3], packed bed reactors [4], rotary kilns [5, 6] and screw dryers [7, 8] that have been widely used in fuel and energy production, food production, and catalyst manufacturing processes. In the production of biofuel, novel screw reactors have recently been developed and employed in several studies [9, 10, 11, 12, 13, 14], and the biofuel production performance is reported to be comparable to fluidized bed reactors [11]. In screw reactors, usually single screw or double screws are installed in a housing, and the rotation of screw(s) mechanically fluidizes loaded particulate matters in a mild state without any requirement of fluidization gas. While most past research focused on the performance of screw reactors in biofuel production, few research has been done to examine granular flow, heat transfer and mass transfer in such reactors. However, understanding the underlying particulate flow and heat transfer physics is essential for reactor design optimization, robust reactor operation and reactor scale-up.

Experimental measurements of heat transfer parameters in particulate flows have met numerous difficulties and it becomes even harder with the existence of moving parts in screw reactors. As an alternative, numerical simulation was sought in previous research either

*Corresponding author

Email addresses: fenglei.qi@uni.lu (Fenglei Qi), markmw@iastate.edu (Mark Mba Wright)

for fundamental studies [15, 16] or evaluations of heat transfer performance in process equipment [5, 17, 18]. In general, there are two methods for modeling particulate flows. The first method is to consider the particulate matter as a continuous medium and mass, momentum and energy equations are built for the solid phase just as for the fluid. This method is called Eulerian method and the difficulty in this method is to formulate an accurate constitutive law accounting for the rheology of particulate matters. The second method is to treat each single particle as a discrete entity and the motion of each entity is resolved following Newton's equations of motion. This method is usually called Discrete Element Method (DEM) and was first proposed by Cundall and Strack [19] to model the hydrodynamics of granular assembly. In the last decades, some efforts were reported to extend DEM to incorporate heat transfer models in order to simulate non-isothermal or reacting particulate flows [3, 17, 20, 21, 22, 23, 24, 25, 26]. Due to the computational cost in tracking each particle, the application of this method is restricted to particulate systems of a few millions of particles. In this research, the DEM was employed to resolve the motion of particles in a screw reactor and particle scale heat transfer models were developed and coupled to the DEM.

Progress has been made in identifying different heat transfer mechanisms in dense particulate flows and various heat transfer models were proposed in the literature. In dense particulate flows, particles have either high frequency to collide with surrounding particles such as in bubbling fluidized beds or have long-time contact with surrounding particles in fixed beds. In addition to convective heat transfer pathways between particles and the moving fluid around the particles, particle-particle interactions were reported to have a non-trivial contribution to the total heat transfer in some situations [27, 28, 29]. Batchelor and O'Brien [30] derived an approximate analytical solution for the heat conduction through two overlapping spherical particles and proposed the conductive heat flux is proportional to the radius of the contacting surface. They also proved that heat conduction is the main pathway

when the fluid around particles is stagnant and the ratio of the particle thermal conductivity to the fluid conductivity is very large ($k_p/k_f \gg 1$). This model has been widely implemented in DEM in later research [20, 24, 26, 27, 31, 32]. In the case of short-time particle collision, the radius of the contacting surface varies quickly and a different model was proposed by Sun and Chen [33] to account for transient heat conduction through the contacting surface. Li et al. [21, 34] applied this model in simulating conductive heat transfer between particle and particle, and particle and wall in pneumatic transport of granular particles. Zhou et al. [35] improved the model through finite element modeling and the model was employed in later DEM modeling [3, 28]. The conductive heat transfer through stagnant interstitial fluids were considered in [20] and the distribution of conductive heat flux by particle-fluid-particle pathway and particle-particle pathway was investigated. The result indicates the conductive heat transfer by the particle-fluid-particle pathway is the dominant contributor when the ratio of particle thermal conductivity to the fluid conductivity is not very large ($k_p/k_f < 1000$). Research of [22, 26, 27, 29, 36] developed heat transfer models for DEM involving both particle-particle conduction and particle-fluid-particle conduction pathways. Models accounting for radiation between particles were also developed in [17, 37, 38] and it was pointed out that the contribution of radiation heat transfer becomes important at high temperature.

Limited research has been carried out to examine particulate flows and heat transfer in screw dryers/reactors. Empirical correlations were used in predicting heat transfer in auger reactors [39, 40] but no proper validation for their models was provided in both research. In order to examine heat transfer mechanisms in granular flows in a double screw reactor [11], a particle-scale heat transfer model involving particle-particle conduction, particle-fluid-particle conduction and particle-particle radiation was developed in this paper. The model was first validated by comparing model predictions with experimental measurements in the study of heat transfer in packed beds. The model was then applied to simulate heat

transfer in granular flows in the double screw reactor and the operation parameter effects on the temperature oscillation, average temperature, temperature probability distribution were evaluated. The heat flux and heat transfer coefficient of biomass particles were also analyzed.

2. Model description

2.1. Double screw reactor

The modeled double screw reactor was designed by Brown [11] and the geometry is shown in Figure 1. Two screws are installed in the trough. The left screw flight is left-handed and the right screw flight is right-handed. As show in the Figure 1 (a), when the left screw is rotating in the clockwise direction and the right screw is rotating in the counter-clockwise direction, the bulk material is pushed forwards from the inlet side to the outlet side along the axial direction. At the cross section, the materials are pumped downwards at the center of the reactor. This material flow pattern in the double screw reactor is often called "Counter-Rotating Down Pumping" [41]. The screw rotation speed varied from 20 RPM to 60 RPM in the operation of reactor [11].

There are two inlets which separately feed biomass particles (red oak) at the inlet 1 and heat carrier particles (sand) at inlet 2 into the reactor as shown in Figure 1 (a). The biomass particle has a particle size range of 300-710 μm in the experiments [11] and is fed into the system at the ambient temperature. The sand particle either has a particle range of 250-600 μm (fine sand) or 600-1000 μm (coarse sand) in the experiments and is fed into the system at high temperature depending on the reaction temperature requirement.

2.2. Discrete element method(DEM)

DEM is a numerical technique that resolves each individual particle motion in a particulate system containing a collection of particles. With regard to particle dynamics, the DEM

model in this work is based on the so-called soft sphere approach that has been implemented in LIGGGHTS [42]. In this approach, particle collision is resolved and contact forces are calculated based on the deformation at the contact point by adopting force-displacement models such as linear spring-dashpot model and Hertz-Mindlin nonlinear model [43]. In this research, we employed the Hertz-Mindlin model which was proposed in [44, 45]. The translational and rotational motion are resolved by numerically integrating Newton's and Euler's equations for spherical particles, written as

$$m_i \frac{d\boldsymbol{v}_i}{dt} = \sum_j \boldsymbol{F}_{ij}^c + \boldsymbol{F}_i^f + \boldsymbol{F}_i^g, \tag{1}$$

$$I_i \frac{d\boldsymbol{w}_i}{dt} = \sum_j \left(\boldsymbol{T}_{t,ij} + \boldsymbol{T}_{r,ij}\right), \tag{2}$$

where, m_i and I_i ($=2/5 m_i R_i^2$) are the mass of particle i and the moment of inertia of the particle, separately. $\boldsymbol{v}_i$ and $\boldsymbol{w}_i$ are the translational and rotational velocities of the particle. The forces in Equation (1) include contact force $\boldsymbol{F}_{ij}^c$ between particle i and surrounding particle j that collides with particle i, drag force acting on particle i by fluid $\boldsymbol{F}_i^f$, and gravitational force $\boldsymbol{F}_i^g$. The torques acting on particle i includes both $\boldsymbol{T}_{t,ij}$ and $\boldsymbol{T}_{r,ij}$. The torque $\boldsymbol{T}_{t,ij}$ is generated by the tangential force $\boldsymbol{F}_{t,ij}^c$ which is the component of the contact force $\boldsymbol{F}_{ij}^c$ with direction parallel to the contacting surface between particle i and j. The torque $\boldsymbol{T}_{r,ij}$, called rolling friction torque, is generated by asymmetric distribution of the normal contact force $\boldsymbol{F}_{n,ij}^c$, the other component of $\boldsymbol{F}_{ij}^c$ with direction perpendicular to the contacting surface. In this research, the drag force is ignored in the bed of double screw reactor since the major forces arise from mechanical torques by the shaft. The mechanical forces are transferred by particle-particle contacts/collisions and particle-wall contacts/collisions in the bed. The equations for calculating the forces and the torques acting on particle i are summarized in Table 1 .

2.3. Particle-scale heat transfer model

In this research, we assume a homogeneous temperature distribution within particles so that no mathematical model is required for resolving intra-particle temperature. The evolution of the temperature T_i for particle i is then calculated as

$$m_i c_{p,i} \frac{dT_i}{dt} = \sum_j Q_{ij}, \tag{3}$$

where, m_i is the mass of the particle, $c_{p,i}$ is the specific heat capacity of the particle, and Q_{ij} is heat transfer rate between particle i and neighbor particle/wall j which includes both conductive heat transfer and heat exchange by radiation between them. The fluid movement relative to the particles is ignored in the screw-driven moving bed and the convective heat transfer between fluid and particles is not considered in this research.

2.3.1. Conductive heat transfer

For the heat conduction due to particle-particle contact as shown in Figure 2 (a), the equation of Batchelor and O'Brien [30] is adopted but a modified coefficient reported in [20] is used:

$$Q_{i,j}^{pp} = \frac{4cr_c(T_j - T_i)}{\frac{1}{k_{p,i}} + \frac{1}{k_{p,j}}}, \tag{4}$$

where, $Q_{i,j}^{pp}$ is conductive heat transfer rate through particle-particle contact surface; r_c is the radius of the contact surface obtained in the DEM simulation; $k_{p,i}$ and $k_{p,j}$ are particle thermal conductivities. In the DEM model, a several orders smaller Young's modulus is usually adopted as a general practice in order to reduce computational cost. The contact radius is overestimated with the smaller Young's modulus in the DEM model which results in overprediction of the conductive heat transfer rate. A coefficient c is incorporated to correct the overestimated contact radius and formulated as [27]

$$c = \left(\frac{E^*}{E_0^*}\right)^{1/5}. \tag{5}$$

In the equation, E^* is the value of Young's modulus used in the DEM model and E_0^* is the real value of Young's modulus of the materials.

Another contribution to the total conductive heat transfer between two particles is by particle-fluid-particle conduction pathway as indicated in Figure 2 in both contacting and noncontacting scenarios. In a particulate bed, a particle has a complicated connection with surrounding particles and the heat transfer with surrounding particles by the particle-fluid-particle conduction is affected by this connection. Cheng et al. [20] proposed a simplified double taper cone model to define particle-fluid-particle heat transfer boundaries for a particle and each of its neighbor particles. As illustrated in Figure 2, AB and $A'B'$ define the heat transfer boundary between particle i and j in both contacting and noncontacting scenarios. The radial position r_{ij} of point C can be determined from particle bed topology such as Voronoi tessellation as formulated in [20]. In this model, we adopted a simplified calculation method which was proposed and validated by Zhou et al. [27] as following:

$$r_{ij} = 0.560R\,(1-\epsilon)^{-\frac{1}{3}}, \tag{6}$$

where ϵ is local porosity, which could be calculated by using grid-based average method. Points A and B are determined from the interception between the line connecting the center of particle and point C and the circular defining the particle surface. It is written as

$$r_{sf} = \frac{R \cdot r_{ij}}{\sqrt{r_{ij}^2 + (R+H)^2}}, \tag{7}$$

The cones O_iAA' and O_jBB' define the conductive heat transfer depth at various radial positions. At radial position r, the interstitial gas film thickness l_g is written as

$$l_g = 2[(R+H) - \sqrt{(R^2 - r^2)}], \tag{8}$$

and the heat transfer depth l_s in the particle is defined as

$$l_s = \sqrt{R^2 - r^2} - r(R+H)/r_{ij}, \tag{9}$$

where R is the particle radius, H is the gap distance between particle i and j, which is equal to $(d_{ij} - 2R)/2$ with d_{ij} being the distance between centers of particle i and j. The gap distance is positive in the noncontacting scenario and it is negative in the contacting scenario. The heat transfer rate calculation due to the particle-fluid-particle pathway is written as:

$$Q_{ij}^{pfp} = (T_j - T_i) \int_{r_{sij}}^{r_{sf}} \frac{2\pi r dr}{l_s \cdot (1/k_{pi} + l/k_{pj}) + l_g/k_f}. \tag{10}$$

In the equation, k_f is the interstitial fluid conductivity. The lower integral limit in Equation (10) is 0 when particles are not in contact and r_c when particles are in contact. The heat flux between two particles is ignored for $H/R > 0.5$ according to [27].

2.3.2. Radiative heat transfer

Cheng et al. [38] proposed a similar double taper cone model for particle-scale radiative heat transfer calculation with additional assumptions. The assumptions are: the spherical particles are opaque and gray emitting; the double taper cone surface $ACBB'C'A'$ in Figure 2 is perfectly insulated and diffusely reflective. In this model, the model geometrical parameters r_{ij} and r_{sf} are determined in the same way as discussed in the above section. Similarly, a cut-off distance was also adopted to determine if the radiative heat transfer between two particles is considered or not. The radiative heat transfer between two particles is ignored for $H/R > 0.5$, which is close to the cut-off distance of 0.48 for short-range radiation as re-

ported in [46]. The simplifications avoid the reconstruction of Voronoi polyhedra every time step and thus reduce computational burden. The treatment was validated in the simulation of heat transfer in packed beds in the following section.

The radiation heat exchange between particle i and j are formulated as:

$$Q_{ij}^{rad} = \frac{\sigma(T_j^4 - T_i^4)}{\frac{1-\epsilon_{r,i}}{\epsilon_{r,i}A_i} + \frac{1}{A_i F_{ij} + [1/(A_i F_{iR}) + 1/(A_j F_{jR})]^{-1}} + \frac{1-\epsilon_{r,j}}{\epsilon_{r,j}A_j}} \tag{11}$$

where, σ is the Stephan-Boltzmann constant $5.6696 \times 10^{-8}\mathrm{W}/(\mathrm{m}^2 \cdot \mathrm{K}^4)$. $\epsilon_{r,i}$ and $\epsilon_{r,j}$ are emissivities of particle i and j. A_i and A_j are the areas of spherical caps AA' and BB' defined by the double taper tape cone model. F_{ij} is the view factor between the two spherical caps. F_{iR} is the view factor between spherical cap AA' of particle i and the double taper cone surface $ACBB'C'A'$, and F_{jR} is the view factor between spherical cap BB' of particle j and the double cone surface $ACBB'C'A'$. According to the definition of the view factor, $F_{ij} + F_{iR} = 1$ and $F_{ji} + F_{jR} = 1$. If the diameters of particle i and j are the same, we have $F_{ij} = F_{ji}$. In this case, the Equation (11) is rewritten as

$$Q_{ij}^{rad} = \frac{\sigma(T_j^4 - T_i^4)}{\frac{1-\epsilon_{r,i}}{\epsilon_{r,i}A_i} + \frac{1-\epsilon_{r,j}}{\epsilon_{r,j}A_j} + \frac{2}{A_i(1+F_{ij})}}. \tag{12}$$

In the equation, view factor F_{ij} is defined as

$$F_{ij} = \frac{1}{A_i}\int_{A_i}\int_{A_j} \frac{\cos\phi_i \cos\phi_j dA_i dA_j}{\pi L^2}, \tag{13}$$

where, L is the distance of the line connecting elements dA_i on A_i and dA_j on A_j. ϕ_i is the angle between the normal of the surface element dA_i and the line while ϕ_j is the angle between the normal of the surface element dA_j and the line.

In this research, correlations for calculating view factors in Equation (11) are built in terms of d_{ij}/R and other parameters in the double taper cone model by using the MONT3D

software [47]. In this software, the Monte Carlo method is used to calculate the view factor between surface elements. The validation of the MONT3D in predicting view factors between two spheres are shown in Figure 3, in which the view factors obtained by using the MONT3D for two identical spheres have a good agreement with theoretical solutions.

In the double taper cone model, the view factor correlation for two noncontacting particles ($0.35 \leqslant \alpha_s \leqslant 0.64$) is formulated as

$$F_{ij} = C_1 \left(\frac{d_{ij}}{R} \right)^{C_2} + C_3, \tag{14}$$

where, C_1, C_2 and C_3 are solely functions of the solid fraction:

$$C_1 = 0.1755 + 6.65\alpha_s,$$
$$C_2 = -0.9373 - 2.899\alpha_s,$$
$$C_3 = -0.2923 + 0.2487\alpha_s,$$

and the correlation for two contacting particles ($0.35 \leqslant \alpha_s \leqslant 0.64$) is correlated in terms of d_{ij}/R as

$$F_{ij} = 0.4\frac{d_{ij}}{R} + 0.215\alpha_s - 0.42. \tag{15}$$

where, d_{ij} is the distance between particle centers. Figure 4 shows the comparisons between the correlation results and predictions from MONT3D. The fitting error between correlations and MONT3D predictions was characterized by standard deviance. The standard deviance of the correlation for noncontacting particles is 0.0058 and 0.0035 for contacting particles. Both correlations have good fittings with MONT3D predictions when the local solid fraction lies within [0.35, 0.64]. It is also observed that the view factor magnitude does not change

significantly with solid fraction varying from 0.4 to 0.6 and the distance between particles has the major influence on the view factor between two particles especially for two noncontacting particles.

According to the categorization proposed by Wu et al. [46], this radiative heat transfer model is a short-range radiation heat transfer model. It was shown that the short-range model could provide good simulation accuracy when the solid conductivity (k_p) is comparable to the effective thermal conductivity of radiation k_r, and the bed temperature is under 1488 K. The biomass material usually has small thermal conductivity (0.1-0.3 $\mathrm{W/(m \cdot K)}$), which satisfies this condition at our concerned temperature range for biomass pyrolysis ($\approx$ 800 K). Our simulations of heat transfer in packed bed also prove this point in the following section.

2.3.3. Particle-wall heat transfer

When the interaction between a particle and an infinite plane wall is detected, Equation (10) can be extended to account for particle-fluid-wall conductive heat transfer in addition to particle-wall conduction through contact surface. The heat transfer model is illustrated in Figure 5 (b). The heat rate is calculated as:

$$Q_{iw}^{pfw} = (T_j - T_w) \int_{r_{siw}}^{r_{sf}} \frac{2\pi r dr}{l_s \cdot (1/k_{pi} + 1/k_w) + l_g/k_f}, \tag{16}$$

where, k_w is the thermal conductivity of the wall, l_g is the thickness of gas film between particle and wall, which is formulated as

$$l_g = (R + H) - \sqrt{(R^2 - r^2)}, \tag{17}$$

and the heat penetration depth in the particle l_s is calculated as

$$l_s = \sqrt{R^2 - r^2} - r(R + H)/r_{ij}, \tag{18}$$

where, H is gap distance between a sphere and a plane wall. The equations (4) and (11) are employed to compute heat-wall conduction through contact surface and radiation, separately, with wall properties substituted for particle j in the equations.

Triangle meshes are usually employed to represent complex surfaces in DEM simulations in order to capture the interactions between particles and walls. The heat transfer between particles and triangle meshes is resolved to predict the heat transfer between particles and surfaces in this research. Figure 5 (a) illustrates some treatments in developing particle-triangle heat transfer model. An effective circular surface is alternatively used to maintain axial symmetry of the heat transfer boundary model for numerical integration simplicity in the Equation (16). The effective circular surface has the same area as the triangle mesh and the effective radius is called r_{eff}. The center of the circular plane D is either located at the contact surface center or at the point in the triangle plane which has the shortest distance to the sphere. The circular surface is adjusted to be perpendicular to the line connecting the center of the circular to the center of the sphere. The upper limit of the integral is either r_{sf} or the radius of the effective circular plane r_{eff} depending on which one is smaller. The view factor between the spherical cap and the effective circular surface can also be developed with MONT3D.

2.4. Parameters in the DEM model

Biomass and sand material properties are listed in Table 2. Properties such as thermal conductivity and specific heat capacity are usually functions of temperature. However, they were kept constant in this study. The ratio of the biomass thermal conductivity to the fluid thermal conductivity is 5:1. The diameters of the biomass and sand particles are equal and the particulate system is a binary mixture in which only particle density is different. The time step in DEM remains 5×10^{-6} which is approximately 5%-6% of Hertz contact time defined as

$$t_{Hertz} = 2.87 \left(\frac{m^*}{v_{rel} R^* (E^*)^2} \right)^{1/5}, \tag{19}$$

where, m^*, R^*, E^* and v_{rel} are defined in Table 1.

Table 3 lists all the operating conditions of cases studied in this paper. The volumetric fill level is calculated following the equation:

$$f = \frac{\pi d_p^3 N/6}{0.56V}, \tag{20}$$

where, d_p is the particle diameter, N is the averaged particle number in one pitch, 0.56 is solid volumetric fraction at very loose random packing, and V is the void space volume in one pitch. We investigated the effects of three parameters including screw rotation speed, reactor volumetric fill level and particle size, on the heat transfer performance of the double screw reactor in this study.

3. Model validation

The particle-scale heat transfer model was implemented in the LIGGGHTS code [42]. In previous research, Cheng et al. [20] and Zhou et al. [27] provided validations for the conduction models applying to both packed beds and fluidized beds. We carried out three additional cases for proving the new implementation of the conduction models and validating the radiation heat transfer model and particle-wall heat transfer model proposed in this paper.

Figure 6 (a) illustrates the first validation case which has similar conditions with the previous experiment study by Vargas and McCarthy [31]. The particles in the simulated system were packed in a hexagonal lattice with 200 rows vertically and 100 columns horizontally. Only one layer of particles was arranged in the depth direction, which makes the simulated system a pseudo 2-D system. The material of the particle is 304 stainless steel with density

of 7930 kg/m^3, heat capacity of 506.0 J/(kg $\cdot$ K), thermal conductivity of 15.0 W/(m $\cdot$ K), Young's modulus of 1.93×10^{11} Pa and Poison ratio of 0.29 [22]. The particle has a diameter of 3 mm and 5 kg load was applied on the top of the bed. The initial temperature of the particles was set to 298.15 K and a fixed temperature of 398.15 was set for the bottom wall of the bed. The other walls were insulated from the ambient.

Figure 6 (b) shows the evolution of average temperature profile with time in the vertical direction from both experimental studies [31] and simulations. The temperature was nondimensionalized with both initial temperature of particles and bottom wall temperature, and the length was nondimensionalized with the height of the bed. The comparison shows that the simulated results have a good agreement with the experimental measurements at time span of 60 minutes and 155 minutes. At time span of 10 minutes, a slight difference was observed between simulation results and experimental measurements which might result from the ideal packing of particles in the simulation comparing to the packing of particles in the experimental facility. A different stress chain will arise due to the differences of particle packing according to [31] and thus affects the heat transfer in the bed. In general, the simulation has a reasonable prediction of the heat transfer in the pseudo 2-D bed system.

Effective Thermal Conductivity (ETC) is often used to evaluate the heat transfer in the packed beds. In a packed bed, the ETC can be calculated as

$$k_e = \frac{q}{(T_h - T_c)/L}, \tag{21}$$

where, q is heat flux with unit of W/m^2; $(T_h - T_c)$ is the temperature difference in the bed and L is heat transfer depth. Previous research has confirmed that the ETC calculation is independent of the cube size sampled from a packed bed when the cube dimension in each direction is greater than 8 particle diameters [20]. The simulated packed bed system for the second and third validation cases is shown in Figure 7 (a). The dimensions of the system

are $13d_p \times 13d_p \times 16d_p$ which is the same as [17]. An unidirectional heat flux is generated by setting a temperature difference between the top wall and the bottom wall and prescribing the other four side surfaces as periodic boundaries. In calculating ETC in Equation (21), the temperature difference is calculated from the top wall and bottom wall temperature. The heating flux q is calculated by summing up heat transfer rates between particles and the bottom wall of the bed and then being divided by the area of the bottom wall.

In the second validation case, the thermal conductivity of the bed particle was varied from 0.8 to 55.0 W/(m $\cdot$ K) while the interstitial fluid conductivity was fixed at 0.02818 W/(m $\cdot$ K). 2890 particles with diameter of 2 mm and density of 1000 kg/m^3 were randomly packed within the cuboid and the bed solid fraction is approximately 0.56. Other parameters used in the model include particle specific heat capacity $C_p = 573.0$ J/(kg $\cdot$ K), Young's Modulus $E = 1 \times 10^7$ Pa, Poisson Ratio $\nu = 0.3$, friction coefficient $\mu = 0.4$, and original Young's Modulus $E_0 = 1 \times 10^{10}$ Pa. The same properties were set for both top and bottom walls. The temperatures of the top wall and the bottom wall were set to 298.15 K and 398.15 K, separately. In addition, both primitive method (mathematical description of geometric planes) and surface discretization method were employed to represent both the top and bottom walls in the simulation with the consideration of testing the particle-triangle heat transfer model introduced in section 2.3. In the surface discretization method, triangle meshes are employed which has an average characteristic length of $0.54d_p$. The mesh size has been studied and shows negligible effects on the predicted ETC.

The calculated ETC was compared with the experimental data collected by Cheng et al. [20] in Figure 7 (b). A good agreement is observed between the predicted ETC and the measured ETC in a wide range of particle thermal conductivities. The particle-triangle heat transfer model shows a similar prediction of ETCs compared to the primitive wall method.

In the third validation case, the temperature of the bottom wall was increased gradually from 498 K to 748 K with an increment of 50 K to test the performance of the heat transfer

model at higher bed temperatures. The temperature of the top wall was 50 K less than the bottom wall and a 50 K temperature difference was maintained for all the simulations. A total of 3095 particles with diameter of 4.76 mm were randomly packed within the cuboid and the bed solid fraction is approximately 0.6. Particle conductivity was set to 1.521 $\mathrm{W/(m \cdot K)}$, the specific capacity was set to 700 $\mathrm{J/(kg \cdot K)}$, the emissivity was 0.9, and all three parameters remained constant for all simulations. The conductivity of the interstitial fluid is fixed at 0.039 $\mathrm{W/(m \cdot K)}$. Other properties of the particle include Young's Modulus $E = 1 \times 10^7$ Pa, Poisson Ratio $\nu = 0.3$, friction coefficient $\mu = 0.4$, and original Young's Modulus $E_0 = 5 \times 10^{10}$ Pa.

The predicted ETC was plotted in terms of bed average temperature in the steady state as shown in Figure 7 (c) and compared with the experimental measurements from Walko and Kato [48]. The predictions from DEM are in agreement with experimental measurements at various temperatures.

4. Results and discussion

4.1. Observations of temperature distribution

Particle and temperature distributions in transverse sections are shown in Figure 8 at different operating conditions. The snapshots of the transverse sections were extracted at the end of each pitch downstream the sand feed inlet. In this study, we observed that the particle distributions at different screw rotation speeds are very similar when the volumetric fill level remained constant [49]. Moreover, the particle temperature distributions in the transverse sections and the variation of the temperature distribution from one axial location to the other are both very similar. For simplicity, only snapshots of particle and temperature distributions at screw rotation speed $\omega = 40$ rpm are shown in Figure 8. It is observed that the particle temperature distribution aligns with the particle distribution. In the first two axial locations L/D = 1.25 and L/D=3.75, hot spots are clearly observed at the location

where sand particles reside and relatively cold spots are observed at the locations occupied by biomass particles in Figure 8 (a) and (b). The particle temperature distribution approaches uniform along the axial direction due to the heat transfer between the sand and biomass particles. Both the hot and cold spots shown at location L/D=1.25 disappear at L/D=8.75.

Figure 8 (b) shows particle and temperature distributions in the transverse sections when a smaller particle size is adopted. Similar distribution patterns are observed for both particle mixing and temperature as in Figure 8 (a) where a larger particle size was modeled with DEM.

Figure 8 (c) shows particle and temperature distributions at low volumetric fill level $f = 0.10$. As shown at L/D=1.25, only a thin layer of biomass particles is fed into the reactor and the heat transfer between the biomass particles and the heat carrier particles is initialized immediately. The particle temperature distribution gets uniform at L/D=3.75 while, by comparison, a clear temperature gradient is observed at the same axial location in Figure 8 (b) at high volumetric fill level ($f = 0.37$).

4.2. Oscillation pattern of temperature profile

The screws shown in Figure 1 rotate at a constant speed and the granular flow in the reactor achieves periodic steady state statistically. In this study, we divided the screw rotation period into a series of successive rotation angles with the initial rotation position set to $\theta = 0^\circ$ as shown in Figure 9. Both biomass and sand particle average temperature at a specific rotation angle was obtained by averaging the realizations sampled at that rotation angle for ten rotation periods. Readers could refer to our previous research [49] for detailed description of our sampling method. The average temperature was non-dimensionalized with the initial temperature of the sand particle and the biomass particle:

$$\langle \tau_\theta \rangle = \frac{\langle T \rangle - T_{b,0}}{T_{s,0} - T_{b,0}}, \tag{22}$$

where, $T_{b,0}$ and $T_{s,0}$ are initial temperatures of biomass particles and sand particles, separately. The non-dimensional biomass initial temperature is 0 according to the definition and the biomass non-dimensional temperature at the thermal equilibrium is approximately 0.88. In the following part of the section, the temperature is non-dimensionalized with Equation 22 unless otherwise specified.

The biomass particle average temperature at each rotation angle $\langle \tau_{b,\theta} \rangle$ is plotted in terms of axial positions in Figure 9. For conciseness, biomass temperature profiles at only three rotation angles are shown. It is seen that biomass particles have been warmed up by the trough wall of the reactor before mixing with the heat carrier particles which are fed at $x/D = 4.0$. Some biomass particles flow backward to the left end of the reactor where higher temperature values are observed in the plots near $x/D = 0$. The oscillation patterns at the three rotation angles are very similar. The temperature profiles oscillate along the axial direction, which reoccurs every screw pitch length ($P/D = 1.25$) and the oscillation amplitude gradually increases along the axial direction after the sand feeding inlet. This oscillation pattern is called spatial oscillation in this research. At a fixed axial position, there exists another oscillation which occurs in a sequence of rotation angles. The oscillation pattern is called temporal oscillation since the oscillation repeats every rotation period. The result also indicates that the biomass particles are not heated uniformly in the reactor at this operating condition.

The temperature oscillations at the initial rotation angle were investigated at different operating conditions as shown in Figure 10. The biomass temperature spatial oscillation patterns at different rotation speeds are similar in terms of oscillation frequency and amplitude when both particle size and reactor volumetric fill level remain constant as shown in Figure 10 (a) - (c). But the biomass temperature increases at a smaller rotation speed as a result of improved biomass and sand mixing duration. The sand temperature profile also has a similar oscillation pattern but the oscillation only starts after the non-dimensional tem-

perature decreases to approximately 0.9 which corresponds to the wall temperature. Figure 10 (c), (e) and (f) illustrate the effects of volumetric fill level on the biomass temperature profile. Increasing volumetric fill level leads to a larger oscillation amplitude but the spatial oscillation remains the same oscillation frequency. Changing particle size has different impacts on the temperature profile when the volumetric fill level varies. At a high volumetric fill level ($f = 0.37$), the particle size seems to have little effect on the temperature oscillation pattern as shown in Figure 10 (c) and (d). At a low volumetric fill level ($f = 0.10$), biomass particles of a smaller size reach thermal equilibrium with heat carrier particles faster than the biomass particles of a larger size. This could be explained by the observations that particle mixing at the low volumetric fill level has little impact on the heat transfer between the biomass particle and the heat carrier particle, and the biomass particle of a smaller size is heated up faster due to increased total surface areas.

4.3. Average temperature profile and probability distribution of temperature

The average temperature of biomass particles was obtained by averaging the realizations sampled from each rotation angle with an increment of 24^o for five rotation periods. The temperature probability distribution was obtained by adopting the same sampling method. The probability density is mathematically calculated by

$$g(\tau) = \frac{n\left(\tau\right)}{N\Delta\tau} \tag{23}$$

where, τ is the non-dimensional temperature, $n\left(\tau\right)$ is the number of sampled particles within $\tau \in \left[\tau - \frac{\Delta\tau}{2}, \tau + \frac{\Delta\tau}{2}\right]$, N is the total number of sampled particles.

The average temperature profiles of the biomass particles are shown in Figure 11. Figure 11 (a) shows that the average temperature profiles at screw rotation speed ranging between 20-60 rpm. The average temperature of the biomass particle increases as the screw rotation speed is reduced. At a smaller rotation speed, the mixing duration between biomass

particles and heat carrier particles is enhanced, which results in an improved average temperature profile. The temperature probability distribution of biomass particles at several axial positions are compared in Figure 12 when the screw rotation speed is varied. It is observed that the temperature variance decreases in the downstream when the screw adopts a rotation speed of 20 rpm. This trend is not observed at increased screw rotation speed. At the downstream location $L/D = 8.75$, biomass particles get a narrower temperature distribution at $\omega = 20$ rpm compared with temperature distributions at $\omega = 40$ rpm and $\omega = 60$ rpm.

The average temperature profiles of the biomass particle with different volumetric fill levels are shown in Figure 11 (b). The average temperature of the biomass particle increases as the volumetric fill level decreases. At a smaller volumetric fill level, the biomass particle has more opportunity to be around sand particles, although the particle mixing does not improve as shown in our previous research [49]. More detailed and complete analysis on how the particle mixing affects the heat transfer will be reported in future research. In addition, the sand particle could regain energy from the reactor wall quickly with a lower volumetric fill level. The variance of biomass particle temperature distribution decreases as the volumetric fill level is reduced, which could be observed from Figure 13. The double screw reactor has a better performance in heating up biomass particles at a lower volumetric fill level.

Figure 11 (c) shows the biomass average temperature profiles of two particle sizes. Results indicate smaller particle size is favorable for gaining a faster heating rate. The ratio of particle surface area to its volume increases as the particle size is decreased and the total heat transfer area between biomass particles and heat carrier particles increases. When the particle size decreases, the comparison of variances of the temperature in Figure 14 shows that the probability density profile shifts slightly to the right at each location, indicating that the probability of particles within a higher temperature range increases.

4.4. Heating flux

As discussed in Section 2.3, the heat is transferred from the sand particles to the biomass particles by three different heat transfer pathways: particle-particle conduction through contact surface, particle-fluid-particle conduction pathways in both contacting and noncontacting scenarios, and particle-particle radiation. Three similar pathways were also considered for the heat transfer from the reactor walls to the enclosed particles. In order to better understand the dominant heat transfer mechanisms in the biomass and sand granular flow, the contribution of different heat transfer pathways to the total heat flux received by the biomass particles from both the sand particles and reactor walls were analyzed and shown in Figure 15. The total heat transfer flux is a key factor for characterizing biomass heating-up process. The heat transfer flux can be compared with that in other types of reactor such as bubbling fluidized bed reactor for performance evaluation.

In Figure 15, the heat fluxes are plotted in terms of the axial position so that the changes of the heat flux in the axial position could be observed. The biomass particle feed inlet is located at $x/D = 2.0$ and the sand particle feed inlet is located at $x/D = 4.0$ as shown in Figure 9. It is observed that adding the heat carrier particles to the reactor enhance the heating fluxes of biomass particle. For example, in Figure 15 (b), heat fluxes by particle-fluid-particle and radiation at location $x/D = 4.0$ is approximately twice of the counterpart heat fluxes at location $x/D = 2.0$. It is also observed that the heat flux seems to increase as x/D decreases from the biomass feed inlet as a result of low local volumetric fill level and direct contact of biomass particles with reactor wall. All heat fluxes from different heat transfer pathways decrease along axial direction as x/D increases from sand feed inlet. The temperature difference between the sand particle and biomass particle decreases as illustrated in Figure 11 which results in the reduction of the heat fluxes. It is also observed that improving screw rotation speed and reducing volumetric fill level could increase the heat flux received by biomass particle. Reducing particle size decreases the heat flux by

each pathway.

The contribution of each heat pathway to the total heat flux indicates little changes within the reactor. The main contribution comes from the particle-fluid-particle heat transfer pathway and both contacting and noncontacting scenarios contribute almost equally except at the low volumetric fill level operating condition. The percentage of particle-fluid-particle heat flux in the total heating flux is approximately 36% for both contacting and noncontacting scenarios as shown in Figure 15 (a) and (b). The percentage increases to around 40% as the particle size is decreased, seen in Figure 15 (d). At low volumetric fill level, the heat flux by contacting particle-fluid-particle heat conduction has a larger contribution to the total heat flux than the heat flux by noncontacting particle-fluid-particle heat conduction. The radiation heat flux is the second contributor to the heating flux which can not be ignored at the investigated operating temperatures. The percentage of the radiation heat flux in the total heating flux is approximately 26% and the percentage decreases to 14% as the particle size decreases from 2 mm to 1 mm. The contribution of the heat flux by heat conduction through particle-particle contact surface or particle-wall contact surface is relatively small and it only accounts for 1% in the total heat flux with particle size of 2 mm and increases to 5% with particle size of 1 mm.

4.5. Heat transfer coefficient (HTC)

The average heat transfer coefficient based on the biomass phase is defined as

$$h = \langle \sum_{j} \frac{q_{bs,ij}}{T_{s,j} - T_{b,i}} \rangle, \tag{24}$$

where, $T_{b,i}$ and $T_{s,j}$ are temperatures of biomass particle i and heat carrier particle j, separately; $q_{bs,ij}$ is heat transfer flux received by biomass particle i from sand particle j; $\langle ... \rangle$ is average operator acting on each particle in the sampling.

Figure 16 shows the breakdown of heat transfer coefficient at different operating condi-

tions. The results illustrate that the feeding of heat carrier particles into the reactor enhances all the heat transfer coefficients including conductive HTC, radiative HTC and total HTC at all operating conditions. At the heat carrier particle feeding location ($x/D \approx 4.0$), the HTCs increase rapidly, for example, the total HTC increases from 26.3 W/(m$^2 \cdot$ K) at $x/D = 2.0$ to 69.4 W/(m$^2 \cdot$ K) at $x/D = 6.0$, the conductive HTC increases from 22.7 W/(m$^2 \cdot$ K) at $x/D = 2.0$ to 52.3 W/(m$^2 \cdot$ K) at $x/D = 6.0$, and the radiative HTC increases from 3.7 W/(m$^2 \cdot$ K) at $x/D = 2.0$ to 17.0 W/(m$^2 \cdot$ K) at $x/D = 6.0$ when the reactor is operated at rotation speed of 40 RPM and volumetric fill level of 0.37 with particle diameter of 2 mm for both biomass and sand particles. All the HTCs remains relatively constant after $x/D = 6.0$ in most cases, which indicates that the heat transfer mechanisms do not change after that position.

The variation of screw rotation speed has smaller effects on the HTCs compared to the effects of volumetric fill level and particle size parameters. Increasing screw rotation speed leads to a decrease of the total heat transfer coefficient, which is mainly due to the reduction of radiative HTC at a higher rotation speed. The conductive HTC has little changes with the variation of screw rotation speed. Decreasing volumetric fill level could enhance all the HTCs as indicated in Figure 16 (b). Reducing particle size in the reactor could also enhance the conductive HTC but reduces the radiative HTC, which altogether results in an increase in the total HTC.

Figure 17 shows the contributions of particle-particle HTC and particle-wall HTC to the total HTC in all operating conditions. The results directly show that the heating-up process of biomass particles is significantly increased by feeding heat carrier particles into the reactor. We observe a decrease of particle-wall HTC with the feeding of heat carrier particles. The heat carrier particles have a larger density which tend to sink to the bottom of the reactor and reduce the contacts/collisions of biomass particles with the bottom surfaces of the reactor, which could explain the decrease of particle-wall HTC. Both the particle-

particle HTC and the particle-wall HTC remain relatively constant after $x/D = 6.0$. From Figure 17 (a), it is observed that increasing screw rotation speed results in decrease of both particle-particle HTC and particle-wall HTC. Reducing particle volumetric fill level could enhance the heating-up process of biomass particle due to increased HTCs. Particle-particle HTC increases with a smaller particle size at the same screw rotation speed and volumetric feed level. However, the particle-wall HTC decreases at a smaller particle size.

5. Conclusion

In this research, a particle-scale heat transfer model was developed in which particle-particle conduction through contact surface, particle-fluid-particle conduction and particle-particle radiation are considered. A particle-wall heat transfer model was also proposed for resolving particle-wall conductive and radiative heat transfer. The developed thermal DEM model was validated by comparing predicted ETCs with experimentally measured ETCs in packed beds. The comparisons validate both the particle-particle conductive and radiative heat transfer models, and the developed particle-wall heat transfer model. The thermal DEM model was applied to simulate the heat transfer in binary component granular flows in the double screw reactor. Both spatial and temporal temperature oscillation patterns are identified in the double screw reactor. The effects of the operating conditions on average temperature profile, biomass particle temperature probability distribution, heat flux and heat transfer coefficient are analyzed. We report that the particle-fluid-particle conductive heat transfer pathways are the dominant contributors to the total heat flux, which accounts for approximately 70%-80% in the total heat flux. Radiative heat transfer contributes 14%-26% to the total heat flux and the conductive heat transfer through contact surface takes only 1%-5% in the total heat flux. The heat transfer coefficient in the double screw reactor is also reported, which varies in a wide range for different operating conditions. The particle mixing has a great impact on the heat transfer in the granular flow. While this paper focuses

more on the heat transfer related parameter analysis, a more in-depth analysis of particle mixing effects on the heat transfer requires further investigation.

Acknowledgements

The research reported in this paper is partially supported by the HPC@ISU equipment at Iowa State University, some of which has been purchased through funding provided by NSF under MRI grant number CNS 1229081 and CRI grant number 1205413.

Funding: This work was supported by the National Science Foundation EPSCoR program [Grant EPS-1101284].

Nomenclature

c	contact radius correction coefficient	l_g	gas film thickness, m
$c_{p,i}$	particle specific heat capacity, $\mathrm{J/(kg \cdot K)}$	l_s	heat penetration depth into particle, m
d	shaft diameter, m	m_i	particle mass, kg
d_{ij}	distance between particle centers	m^*	particle equivalent mass, kg
d_p	particle diameter, m	$\dot{m}$	mass feeding rate, kg/h
D	screw flight diameter, m	$\hat{\boldsymbol{n}}_{ij}$	unit vector in the normal direction
e	coefficient of restitution	P	screw pitch length, m
E_i	Young's modulus, Pa	Q_{ij}	heat transfer rate between particles, J/s
E^*	equivalent Young's modulus, Pa	Q_{ij}^{pfp}	heat transfer rate by particle-fluid-particle pathway, J/s

f	volumetric fill level	Q_{ij}^{pp}	heat transfer rate by particle-particle pathway, J/s
F_{ij}	view factor between surfaces	Q_{ij}^{rad}	heat transfer rate by radiation pathway, J/s
$\boldsymbol{F}_i^f$	drag force acting on particle i, N	R_i	radius of particle, m
$\boldsymbol{F}_i^g$	gravitational force acting on particle i, N	R^*	particle equivalent radius, m
$\boldsymbol{F}_{ij}^c$	particle collision force, N	r_c	radius of contact surface, m
$\boldsymbol{F}_{n,ij}^c$	normal collision force, N	t_{Hertz}	Hertz contact time, s
$\boldsymbol{F}_{t,ij}^c$	tangential collision force, N	$\hat{\boldsymbol{t}}_{ij}$	tangential unit vector
G_i	particle shear modulus, Pa	T_i	particle temperature, K
G^*	equivalent shear modulus, Pa	$\boldsymbol{T}_{r,ij}$	rolling friction torque, $\mathrm{N}\cdot\mathrm{m}$
h	heat transfer coefficient, $\mathrm{W}/(\mathrm{m}^2\cdot\mathrm{K})$	$\boldsymbol{T}_{t,ij}$	tangential torque, $\mathrm{N}\cdot\mathrm{m}$
H	gap between particles, m	$\boldsymbol{v}_i$	particle velocity, m/s
I_i	particle moment of inertia, $\mathrm{kg}\cdot\mathrm{m}^2$	$\boldsymbol{v}_{rel}$	particle relative velocity, m/s
k_f	fluid thermal conductivity, $\mathrm{W}/(\mathrm{m}\cdot\mathrm{K})$	$\boldsymbol{v}_{n,rel}$	relative velocity in the normal direction, m/s
$k_{p,i}$	particle thermal conductivity, $\mathrm{W}/(\mathrm{m}\cdot\mathrm{K})$	$\boldsymbol{v}_{t,rel}$	relative velocity in the tangential direction, m/s
k_w	reactor wall thermal conductivity, $\mathrm{W}/(\mathrm{m}\cdot\mathrm{K})$	x	axial position in the reactor, m
L	screw mixing length, m		

Greek symbols

α_s	solid fraction	μ_r	rolling friction coefficient

β	damping coefficient	ν	Poisson's ratio
δ_n	particle overlap in the normal direction, m	σ	Stephan-Boltzmann constant, $\mathrm{W}/(\mathrm{m}^2 \cdot \mathrm{K}^4)$
δ_t	particle overlap in the tangential direction, m	τ	non-dimensional temperature
ϵ	porosity	$\boldsymbol{\omega}_i$	particle rotation velocity, rad/s
ϵ_r	radiation emissivity	ω	screw rotating velocity, rad/s
μ	friction coefficient		

Subscripts

b	biomass particles	r	radiation or rolling friction
f	fluid phase	s	sand particles or solid phase
n	normal direction	t	tangential direction
p	particle	θ	rotation angle

References

[1] J. Chang, G. Wang, J. Gao, K. Zhang, H. Chen, Y. Yang, CFD modeling of particle–particle heat transfer in dense gas-solid fluidized beds of binary mixture, Powder technology 217 (2012) 50–60.

[2] M. Oevermann, S. Gerber, F. Behrendt, Euler–Lagrange/DEM simulation of wood gasification in a bubbling fluidized bed reactor, Particuology 7 (4) (2009) 307–316.

[3] Y. Geng, D. Che, An extended DEM–CFD model for char combustion in a bubbling fluidized bed combustor of inert sand, Chemical Engineering Science 66 (2) (2011) 207–219.

[4] R. Mehrabian, A. Shiehnejadhesar, R. Scharler, I. Obernberger, Multi-physics modelling of packed bed biomass combustion, Fuel 122 (2014) 164–178.

[5] B. Chaudhuri, F. J. Muzzio, M. S. Tomassone, Experimentally validated computations of heat transfer in granular materials in rotary calciners, Powder Technology 198 (1) (2010) 6–15.

[6] Y. Gao, B. J. Glasser, M. G. Ierapetritou, A. Cuitino, F. J. Muzzio, J. W. Beeckman, N. A. Fassbender, W. G. Borghard, Measurement of residence time distribution in a rotary calciner, AIChE Journal 59 (11) (2013) 4068–4076.

[7] S. Waje, B. Thorat, A. Mujumdar, An experimental study of the thermal performance of a screw conveyor dryer, Drying technology 24 (3) (2006) 293–301.

[8] A. Al-Kassir, J. Gañan, F. Tinaut, Theoretical and experimental study of a direct contact thermal screw dryer for biomass residues, Applied thermal engineering 25 (17) (2005) 2816–2826.

[9] M. Day, Z. Shen, J. Cooney, Pyrolysis of auto shredder residue: experiments with a laboratory screw kiln reactor, Journal of Analytical and Applied Pyrolysis 51 (1) (1999) 181–200.

[10] S. Kelkar, C. M. Saffron, L. Chai, J. Bovee, T. R. Stuecken, M. Garedew, Z. Li, R. M. Kriegel, Pyrolysis of spent coffee grounds using a screw-conveyor reactor, Fuel Processing Technology 137 (2015) 170–178.

[11] J. N. Brown, Development of a lab-scale auger reactor for biomass fast pyrolysis and process optimization using response surface methodology, Master's thesis, Iowa State University, Ames, Iowa, USA (2009).

[12] L. Ingram, D. Mohan, M. Bricka, P. Steele, D. Strobel, D. Crocker, B. Mitchell, J. Mohammad, K. Cantrell, C. U. Pittman Jr, Pyrolysis of wood and bark in an auger reactor: physical properties and chemical analysis of the produced bio-oils, Energy & Fuels 22 (1) (2007) 614–625.

[13] S.-S. Liaw, Z. Wang, P. Ndegwa, C. Frear, S. Ha, C.-Z. Li, M. Garcia-Perez, Effect of pyrolysis temperature on the yield and properties of bio-oils obtained from the auger pyrolysis of Douglas Fir wood, Journal of Analytical and Applied Pyrolysis 93 (2012) 52–62.

[14] N. Puy, R. Murillo, M. V. Navarro, J. M. López, J. Rieradevall, G. Fowler, I. Aranguren, T. García, J. Bartrolí, A. M. Mastral, Valorisation of forestry waste by pyrolysis in an auger reactor, Waste management 31 (6) (2011) 1339–1349.

[15] B. Sun, S. Tenneti, S. Subramaniam, Modeling average gas–solid heat transfer using particle-resolved direct numerical simulation, International Journal of Heat and Mass Transfer 86 (2015) 898–913.

[16] Z.-G. Feng, S. G. Musong, Direct numerical simulation of heat and mass transfer of spheres in a fluidized bed, Powder Technology 262 (2014) 62–70.

[17] Z. Zhou, A. Yu, P. Zulli, A new computational method for studying heat transfer in fluid bed reactors, Powder Technology 197 (1) (2010) 102–110.

[18] H. Kruggel-Emden, S. Wirtz, E. Simsek, V. Scherer, Modeling of granular flow and combined heat transfer in hoppers by the discrete element method (DEM), Journal of Pressure Vessel Technology 128 (3) (2006) 439–444.

[19] P. A. Cundall, O. D. Strack, A discrete numerical model for granular assemblies, Geotechnique 29 (1) (1979) 47–65.

[20] G. Cheng, A. Yu, P. Zulli, Evaluation of effective thermal conductivity from the structure of a packed bed, Chemical Engineering Science 54 (19) (1999) 4199–4209.

[21] J. Li, D. Mason, A computational investigation of transient heat transfer in pneumatic transport of granular particles, Powder Technology 112 (3) (2000) 273–282.

[22] W. L. Vargas, J. McCarthy, Conductivity of granular media with stagnant interstitial fluids via thermal particle dynamics simulation, International Journal of Heat and Mass Transfer 45 (24) (2002) 4847–4856.

[23] W. Siu, S.-K. Lee, Transient temperature computation of spheres in three-dimensional random packings, International journal of heat and mass transfer 47 (5) (2004) 887–898.

[24] B. Chaudhuri, F. J. Muzzio, M. S. Tomassone, Modeling of heat transfer in granular flow in rotating vessels, Chemical Engineering Science 61 (19) (2006) 6348–6360.

[25] Y. Feng, K. Han, D. Owen, Discrete thermal element modelling of heat conduction in particle systems: Pipe-network model and transient analysis, Powder Technology 193 (3) (2009) 248–256.

[26] T. Tsory, N. Ben-Jacob, T. Brosh, A. Levy, Thermal DEM–CFD modeling and simulation of heat transfer through packed bed, Powder technology 244 (2013) 52–60.

[27] Z. Zhou, A. Yu, P. Zulli, Particle scale study of heat transfer in packed and bubbling fluidized beds, AIChE Journal 55 (4) (2009) 868–884.

[28] J. Chang, S. Yang, K. Zhang, A particle-to-particle heat transfer model for dense gas–solid fluidized bed of binary mixture, Chemical Engineering Research and Design 89 (7) (2011) 894–903.

[29] W. Yang, Z. Zhou, A. Yu, Particle scale studies of heat transfer in a moving bed, Powder Technology 281 (2015) 99–111.

[30] G. Batchelor, R. O'brien, Thermal or electrical conduction through a granular material, in: Proceedings of the Royal Society of London A: Mathematical, Physical and Engineering Sciences, Vol. 355, The Royal Society, 1977, pp. 313–333.

[31] W. L. Vargas, J. McCarthy, Heat conduction in granular materials, AIChE Journal 47 (5) (2001) 1052–1059.

[32] A. R. Amritkar, D. Tafti, S. Deb, Particle scale heat transfer analysis in rotary kiln, in: ASME 2012 Heat Transfer Summer Conference collocated with the ASME 2012 Fluids Engineering Division Summer Meeting and the ASME 2012 10th International Conference on Nanochannels, Microchannels, and Minichannels, American Society of Mechanical Engineers, 2012, pp. 953–962.

[33] J. Sun, M. Chen, A theoretical analysis of heat transfer due to particle impact, International Journal of Heat and Mass Transfer 31 (5) (1988) 969–975.

[34] J. Li, D. J. Mason, A. S. Mujumdar, A numerical study of heat transfer mechanisms in gas–solids flows through pipes using a coupled CFD and DEM model, Drying Technology 21 (9) (2003) 1839–1866.

[35] J. Zhou, A. Yu, M. Horio, Finite element modeling of the transient heat conduction between colliding particles, Chemical Engineering Journal 139 (3) (2008) 510–516.

[36] T. Oschmann, M. Schiemann, H. Kruggel-Emden, Development and verification of a resolved 3D inner particle heat transfer model for the discrete element method (DEM), Powder Technology 291 (2016) 392–407.

[37] E. Simsek, B. Brosch, S. Wirtz, V. Scherer, F. Krüll, Numerical simulation of grate firing systems using a coupled CFD/discrete element method (DEM), Powder technology 193 (3) (2009) 266–273.

[38] G. Cheng, A. Yu, Particle scale evaluation of the effective thermal conductivity from the structure of a packed bed: Radiation heat transfer, Industrial & Engineering Chemistry Research 52 (34) (2013) 12202–12211.

[39] S. Aramideh, Q. Xiong, S.-C. Kong, R. C. Brown, Numerical simulation of biomass fast pyrolysis in an auger reactor, Fuel 156 (2015) 234–242.

[40] H. B. OSMAN, Granular flow and heat transfer in a screw conveyor heater: a discrete element modeling study, Master's thesis, National University of Singapore, Singapore (2012).

[41] T. A. Kingston, T. J. Heindel, Granular mixing optimization and the influence of operating conditions in a double screw mixer, Powder Technology 266 (2014) 144–155.

[42] C. Kloss, C. Goniva, A. Hager, S. Amberger, S. Pirker, Models, algorithms and validation for opensource DEM and CFD–DEM, Progress in Computational Fluid Dynamics, an International Journal 12 (2-3) (2012) 140–152.

[43] H. Zhu, Z. Zhou, R. Yang, A. Yu, Discrete particle simulation of particulate systems: theoretical developments, Chemical Engineering Science 62 (13) (2007) 3378–3396.

[44] H. Hertz, Über die berührung fester elastischer körper., Journal für die reine und angewandte Mathematik 92 (1882) 156–171.

[45] R. D. Mindlin, H. Deresiewica, Elastic spheres in contact under varying oblique forces, Journal of applied mechanics 20.

[46] H. Wu, N. Gui, X. Yang, J. Tu, S. Jiang, Effect of scale on the modeling of radiation heat transfer in packed pebble beds, International Journal of Heat and Mass Transfer 101 (2016) 562–569.

[47] C. Zeeb, P. Burns, K. Branner, J. Dolaghan, User's manual for mont 3d-version 2.4, Colorado State University, Fort Collins, CO.

[48] N. Wakao, K. Kato, Effective thermal conductivity of packed beds, Journal of Chemical Engineering of Japan 2 (1) (1969) 24–33.

[49] F. Qi, T. J. Heindel, M. M. Wright, Numerical study of particle mixing in a lab-scale screw mixer using the discrete element method, Powder Technology 308 (2017) 334–345.

Table 1: Equations for calculating contact forces and torques in DEM

Force or torque	Equation
Normal force $\boldsymbol{F}^c_{n,ij}$	$-\frac{4}{3}E^*\sqrt{R^*}\delta_n^{3/2}\hat{\boldsymbol{n}}_{ij} - \sqrt{\frac{20}{3}}\beta\left(m^*E^*\sqrt{R^*\delta_n}\right)^{1/2}\boldsymbol{v}_{n,rel}$
Tangential force $\boldsymbol{F}^c_{t,ij}$	$\boldsymbol{min}\{-8G^*\sqrt{R^*\delta_n}\delta_t\hat{\boldsymbol{t}}_{ij} + \sqrt{\frac{20}{3}}\beta\left(4m^*G^*\sqrt{R^*\delta_n}\right)^{1/2}\boldsymbol{v}_{t,rel},\ -\mu\lvert\boldsymbol{F}^c_{n,ij}\rvert\hat{\boldsymbol{t}}_{ij}\}$
Torque $\boldsymbol{T}_{t,ij}$	$\boldsymbol{R}_i \times \boldsymbol{F}^c_{t,ij}$
Torque $\boldsymbol{T}_{r,ij}$	$-\frac{4}{3}\mu_r E^* R^* \sqrt{R^*}\delta_n^{3/2}\boldsymbol{\omega}_{rel}/\lvert\boldsymbol{\omega}_{rel}\rvert$

where, $\frac{1}{m*} = \frac{1}{m_i} + \frac{1}{m_j}$, $\frac{1}{R*} = \frac{1}{R_i} + \frac{1}{R_j}$, $\frac{1}{E*} = \frac{\left(1-\nu_i^2\right)}{E_i} + \frac{\left(1-\nu_j^2\right)}{E_j}$
$\frac{1}{G*} = \frac{2(2-\nu_i)(1+\nu_i)}{G_i} + \frac{2(2-\nu_j)(1+\nu_j)}{G_j}$, $\beta = \ln(\mathrm{e})/\sqrt{\ln^2(\mathrm{e}) + \pi^2}$
$\hat{\boldsymbol{n}}_{ij} = (\boldsymbol{x}_j - \boldsymbol{x}_i)/|\boldsymbol{x}_j - \boldsymbol{x}_i|$, $\boldsymbol{v}_{rel} = \boldsymbol{v}_j - \boldsymbol{v}_i + \boldsymbol{\omega}_j \times \boldsymbol{R}_j - \boldsymbol{\omega}_i \times \boldsymbol{R}_i$,
$\boldsymbol{\omega}_{rel} = \boldsymbol{\omega}_i - \boldsymbol{\omega}_j$, $\boldsymbol{v}_{n,rel} = (\boldsymbol{v}_{rel} \cdot \hat{\boldsymbol{n}}_{ij})\hat{\boldsymbol{n}}_{ij}$, $\boldsymbol{v}_{t,rel} = (\boldsymbol{v}_{rel} \times \hat{\boldsymbol{n}}_{ij}) \times \hat{\boldsymbol{n}}_{ij}$,
$\boldsymbol{R}_i = R_i\hat{\boldsymbol{n}}_{ij}$

Table 2: Biomass and sand properties in DEM

Material*	Red oak	Sand	Steel
Material mechanical properties			
Density ρ (kg/m^3)	550	2680	-
Diameter d_p (mm)	Varied	Varied	-
Young's Modulus E (Pa)	6.0×10^6	6.0×10^6	6.0×10^6
Original Young's Modulus E_o (Pa)	1.2×10^{10}	7.0×10^{10}	2.0×10^{11}
Poisson's ratio ν	0.29	0.25	0.3
Coefficient of restitution e †	0.4	0.65	0.65
Coefficient of friction μ	0.2		
Coefficient of rolling friction μ_r	1×10^{-4}		
Material thermal properties			
Initial Temperature T_0 (K)	300	844	788
Conductivity k $\left(\frac{\mathrm{W}}{\mathrm{m \cdot K}}\right)$ ‡	0.2	1.3	38
Specific heat capacity c_p $\left(\frac{\mathrm{J}}{\mathrm{kg \cdot K}}\right)$	2023	730	490
Emissivity ϵ_r	0.9	0.8	0.8

* Red oak is the material for biomass particles and sand for heat carrier particles. Steel is used for reactor structure.

† This row shows the coefficient of restitution between the same material. The coefficient between red oak and sand is 0.4. The coefficient between red oak and steel is 0.4. The coefficient between sand and steel is 0.65.

‡ The fluid thermal conductivity is 0.039 W/(m · K).

Table 3: Simulation design for heat transfer study in screw reactors

Case No.	Rotation speed ω (rpm)	Particle diameter d_p (mm)	Biomass feed rate $\dot{m}$ (kg/h)	Volumetric fill level f
1	20	2.0	1.75	0.37 (High)
2	40	2.0	3.50	0.37 (High)
3	60	2.0	5.00	0.37 (High)
4	40	1.0	3.50	0.37 (High)
5	40	1.0	1.00	0.10 (Low)
6	40	2.0	2.00	0.20 (Medium)
7	40	2.0	1.00	0.10 (Low)

Figure 1. Geometry of the double screw reactor. Biomass particles are fed into the reactor at inlet 1 and sand particles are fed into the reactor at inlet 2. Reactor dimensions include mixing length L, width W, height H, shaft center distance S, screw flight diameter D, screw pitch P and shaft diameter d. Screws rotate in opposite directions pumping down particles at the center of the reactor (Counter-Rotating Down Pumping). The ratio of the mixing length L to the screw flight diameter D is 10 in this study. The ratio of the screw pitch P to the screw flight diameter D remains 1.25.

Figure 2. Illustration of conductive heat transfer pathways between two particles (a) in contact and (b) not in contact.

Figure 3. Comparison of view factors calculated from MONT3D and theoretical solutions. Theoretical solution for two identical spheres: $F = \frac{1}{\pi C}\int_0^{\frac{\pi}{2}} \frac{2\theta - \sin(2\theta)}{\sqrt{C^2 - 4\cos^2(\theta)}} \sin(2\theta) d\theta$ [46].

Figure 4. View factors of particles (a) in contact and (b) particles not in contact under the double taper cone model. Symbols represent the predictions from the MONT3D and lines are plots of formulated correlations.

Figure 5. Illustration of particle-triangle heat transfer model. (a) effective circular surface; (b) heat transfer model. Dash lines show the effective circular surface having the same area as the triangle ABC.

Figure 6. Validation case 1. (a) Pseudo 2-D packed bed system; (b) Comparison of

average temperature profile evolution with time in the experiment and simulation.

Figure 7. Validation case 2 and 3. (a) 3-D packed bed system; (b) Comparison of DEM predicted ETC with experimentally measured ETC at low temperature; (c) Comparison of DEM predicted ETC with experimentally measured ETC at medium temperature. A primitive wall is a geometrical surface described mathematically and the meshed wall method represents the geometrical wall with a set of triangles.

Figure 8. Snapshots of particle and temperature distributions in transverse sections. The operating conditions are (a) particle diameter $d_p = 2$ mm, volumetric fill level $f = 0.37$ and screw rotation speed $\omega = 40$ rpm, (b) $d_p = 1$ mm, $f = 0.37$ and $\omega = 40$ rpm, (c) $d_p = 1$ mm, $f = 0.10$ and $\omega = 40$ rpm. The first row and second row illustrate particle distribution and temperature distribution at location L/D, respectively. Blue represents the biomass particle and red for the sand particle in the first row in each case.

Figure 9. Temperature profile in the axial direction at different rotation angles. Operating condition: particle diameter $d_p = 2$ mm, volumetric fill level $f = 0.37$ and screw rotation speed $\omega = 40$ rpm.

Figure 10. Temperature profiles in the axial direction at operating condition: (a) screw rotation speed $\omega = 20$ rpm, volumetric fill level $f = 0.37$ and particle size $d_p = 2$ mm; (b) $\omega = 60$ rpm, $f = 0.37$ and $d_p = 2$ mm; (c) $\omega = 40$ rpm, $f = 0.37$ and $d_p = 2$ mm; (d) $\omega = 40$ rpm, $f = 0.37$ and $d_p = 1$ mm; (e) $\omega = 40$ rpm, $f = 0.20$ and $d_p = 2$ mm; (f) $\omega = 40$ rpm, $f = 0.10$ and $d_p = 2$ mm; (g) $\omega = 40$ rpm, $f = 0.10$ and $d_p = 1$ mm; Red triangle lines and blue diamond lines plot the sand particle temperature and the biomass

particle temperature, separately. Gray dash line in (a) shows the sand feed inlet.

Figure 11. Average temperature profiles of biomass particles in the axial direction. (a) $f = 0.37$ and $d_p = 2$ mm; (b) $\omega = 40$ rpm and $d_p = 2$ mm; (c) $\omega = 40$ rpm and $f = 0.37$.

Figure 12. Probability distribution of the biomass particle temperature at screw rotation speed (a) $\omega = 20$ rpm, (b) $\omega = 40$ rpm and (c) $\omega = 60$ rpm. L/D is the axial distant from the sand feed inlet.

Figure 13. Probability distribution of the biomass particle temperature with volumetric fill level (a) $f = 0.10$, (b) $f = 0.20$ and (c) $f = 0.37$. L/D is the axial distant from the sand feed inlet.

Figure 14. Probability distribution of the biomass particle temperature with particle size (a) $d_p = 1.0$ mm and (b) $d_p = 2.0$ mm. L/D is the axial distant from the sand feed inlet.

Figure 15. Contribution of different heat transfer pathways. Operating condition: (a) $\omega = 40$ rpm, $f = 0.37$ and $d_p = 2$ mm; (b) $\omega = 60$ rpm, $f = 0.37$ and $d_p = 2$ mm; (c) $\omega = 40$ rpm, $f = 0.10$ and $d_p = 2$ mm; (d) $\omega = 40$ rpm, $f = 0.37$ and $d_p = 1$ mm. pp refers to heat conduction through particle-particle contact pathway and pfp refers to particle-fluid-particle heat transfer pathway.

Figure 16. Conductive and radiative heat transfer coefficients in the reactor. Other operation conditions: (a) $f = 0.37$ and $d_p = 2$ mm; (b) $\omega = 40$ rpm and $d_p = 2$ mm; (c)

$\omega = 40$ rpm and $f = 0.37$.

Figure 17. Particle-particle (P-P) and particle-wall (P-W) heat transfer coefficients. Other operation conditions: (a) $f = 0.37$ and $d_p = 2$ mm; (b) $\omega = 40$ rpm and $d_p = 2$ mm; (c) $\omega = 40$ rpm and $f = 0.37$.

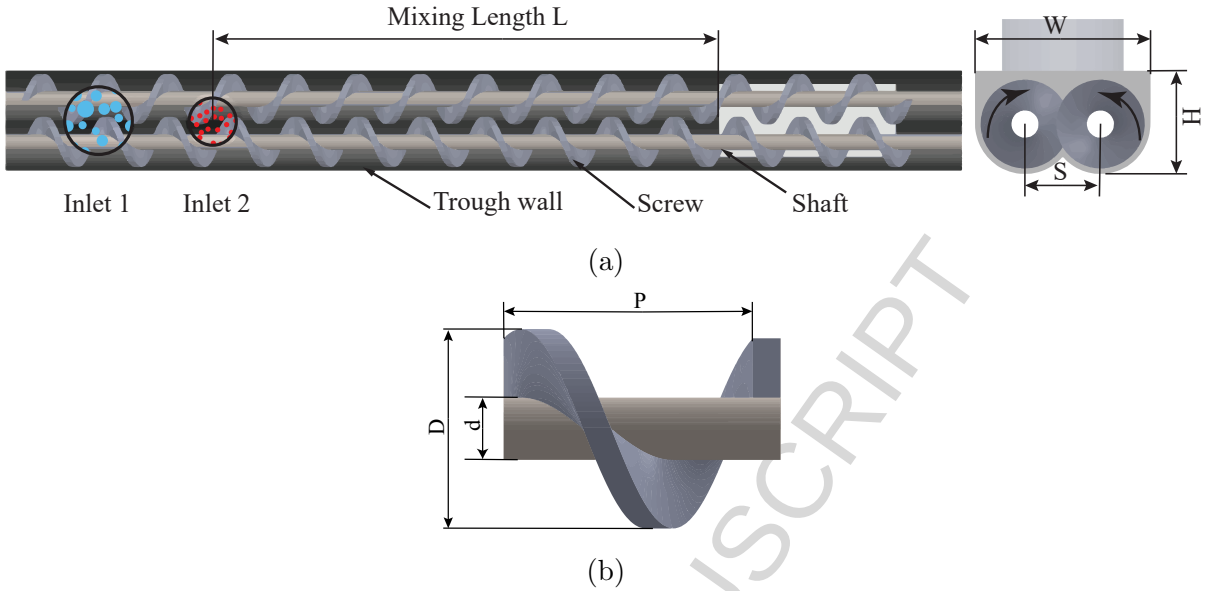

Figure 1: Geometry of the double screw reactor. Biomass particles are fed into the reactor at inlet 1 and sand particles are fed into the reactor at inlet 2. Reactor dimensions include mixing length L, width W, height H, shaft center distance S, screw flight diameter D, screw pitch P and shaft diameter d. Screws rotate in opposite directions pumping down particles at the center of the reactor (Counter-Rotating Down Pumping). The ratio of the mixing length L to the screw flight diameter D is 10 in this study. The ratio of the screw pitch P to the screw flight diameter D remains 1.25.

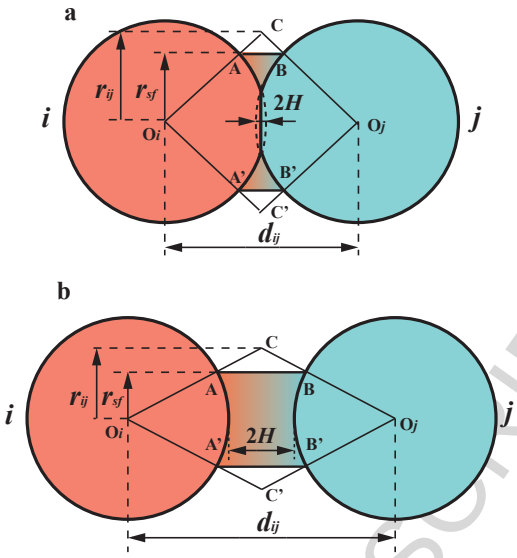

Figure 2: Illustration of conductive heat transfer pathways between two particles (a) in contact and (b) not in contact.

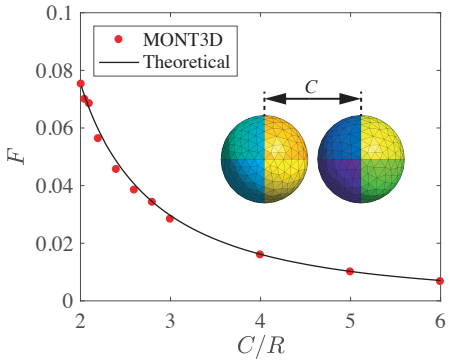

Figure 3: Comparison of view factors calculated from MONT3D and theoretical solutions. Theoretical solution for two identical spheres: $F = \frac{1}{\pi C}\int_0^{\frac{\pi}{2}} \frac{2\theta - \sin(2\theta)}{\sqrt{C^2 - 4\cos^2(\theta)}} \sin(2\theta) d\theta$ [46].

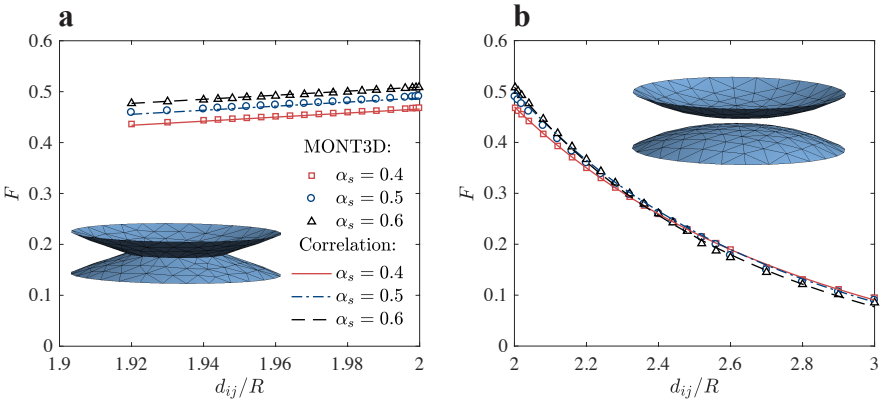

Figure 4: View factors of particles (a) in contact and (b) particles not in contact under the double taper cone model. Symbols represent the predictions from the MONT3D and lines are plots of formulated correlations.

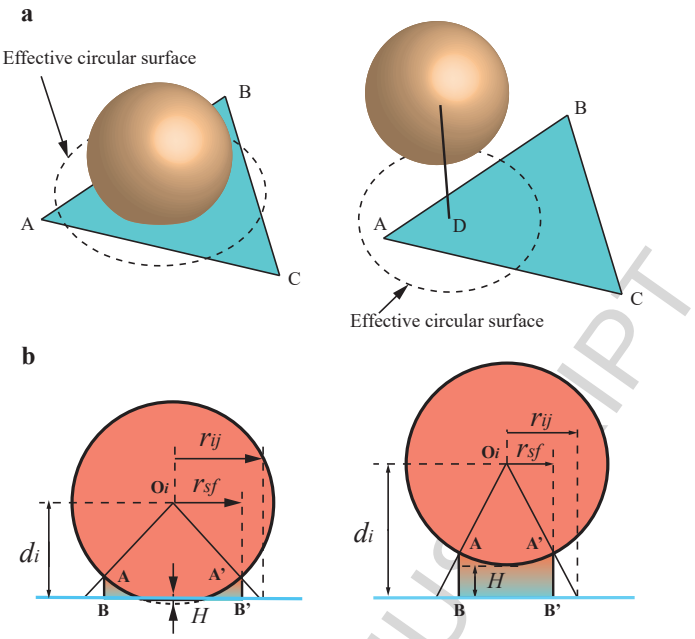

Figure 5: Illustration of particle-triangle heat transfer model. (a) effective circular surface; (b) heat transfer model. Dash lines show the effective circular surface having the same area as the triangle ABC.

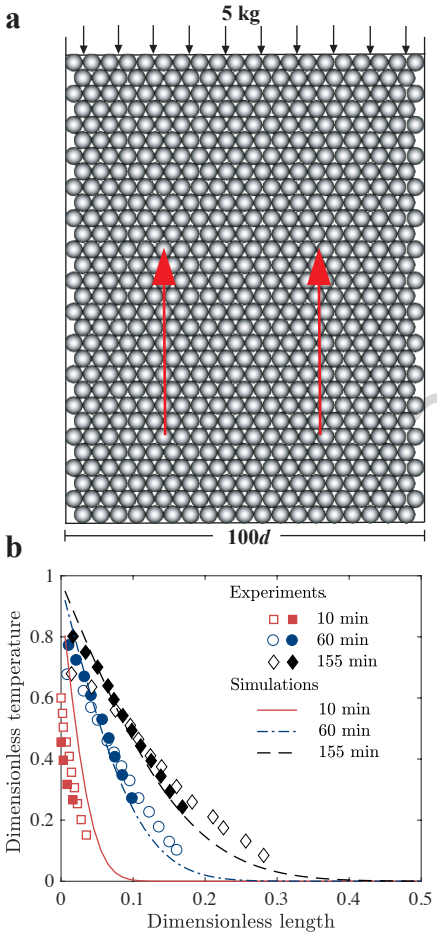

Figure 6: Validation case 1. (a) Pseudo 2-D packed bed system; (b) Comparison of average temperature profile evolution with time in the experiment and simulation.

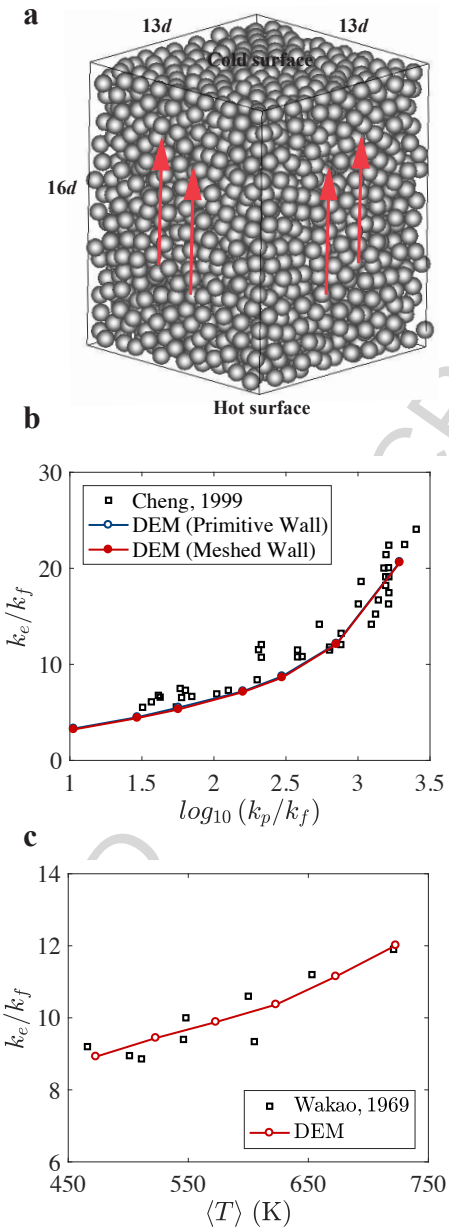

Figure 7: Validation case 2 and 3. (a) 3-D packed bed system; (b) Comparison of DEM predicted ETC with experimentally measured ETC at low temperature; (c) Comparison of DEM predicted ETC with experimentally measured ETC at medium temperature. A primitive wall is a geometrical surface described mathematically and the meshed wall method represents the geometrical wall with a set of triangles.

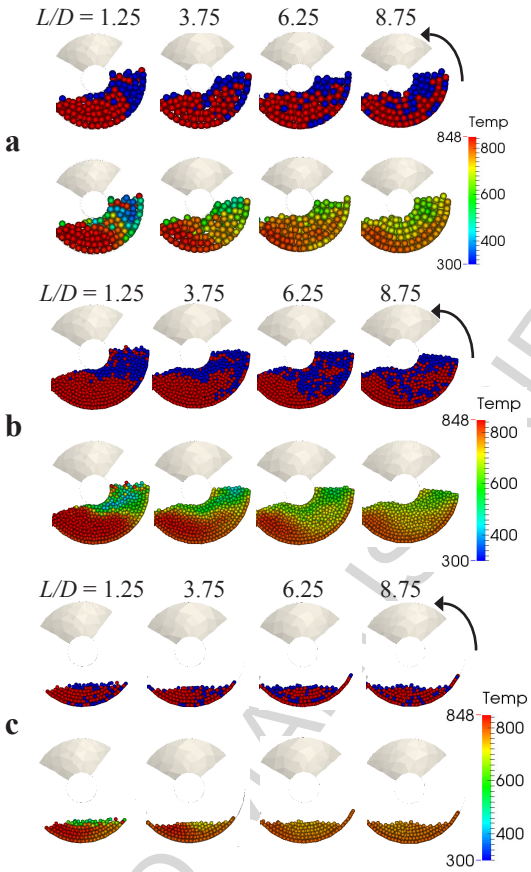

Figure 8: Snapshots of particle and temperature distributions in transverse sections. The operating conditions are (a) particle diameter $d_p = 2$ mm, volumetric fill level $f = 0.37$ and screw rotation speed $\omega = 40$ rpm, (b) $d_p = 1$ mm, $f = 0.37$ and $\omega = 40$ rpm, (c) $d_p = 1$ mm, $f = 0.10$ and $\omega = 40$ rpm. The first row and second row illustrate particle distribution and temperature distribution at location L/D, respectively. Blue represents the biomass particle and red for the sand particle in the first row in each case.

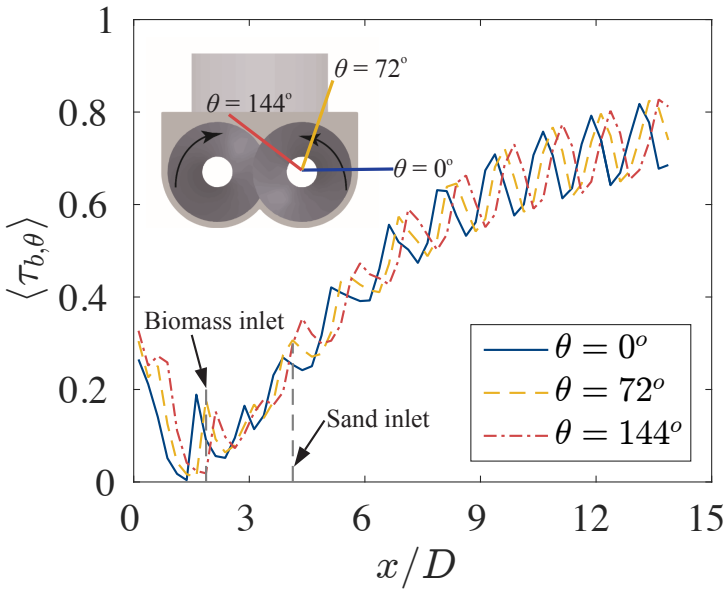

Figure 9: Temperature profile in the axial direction at different rotation angles. Operating condition: particle diameter $d_p = 2$ mm, volumetric fill level $f = 0.37$ and screw rotation speed $\omega = 40$ rpm.

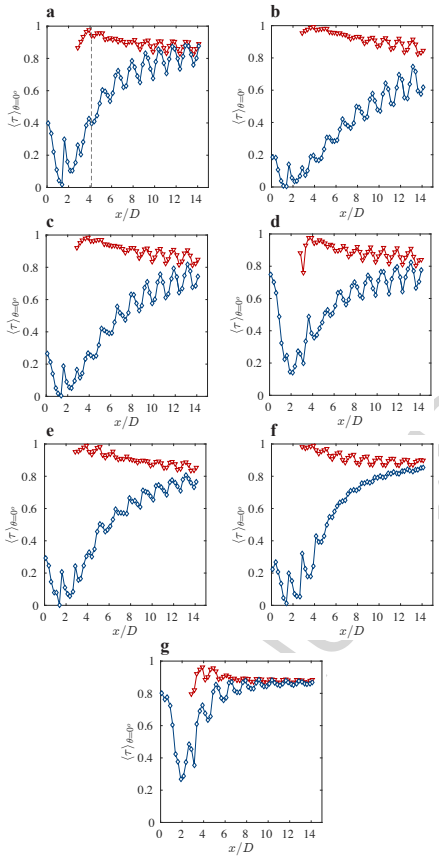

Figure 10: Temperature profiles in the axial direction at operating condition: (a) screw rotation speed $\omega = 20$ rpm, volumetric fill level $f = 0.37$ and particle size $d_p = 2$ mm; (b) $\omega = 60$ rpm, $f = 0.37$ and $d_p = 2$ mm; (c) $\omega = 40$ rpm, $f = 0.37$ and $d_p = 2$ mm; (d) $\omega = 40$ rpm, $f = 0.37$ and $d_p = 1$ mm; (e) $\omega = 40$ rpm, $f = 0.20$ and $d_p = 2$ mm; (f) $\omega = 40$ rpm, $f = 0.10$ and $d_p = 2$ mm; (g) $\omega = 40$ rpm, $f = 0.10$ and $d_p = 1$ mm; Red triangle lines and blue diamond lines plot the sand particle temperature and the biomass particle temperature, separately. Gray dash line in (a) shows the sand feed inlet.

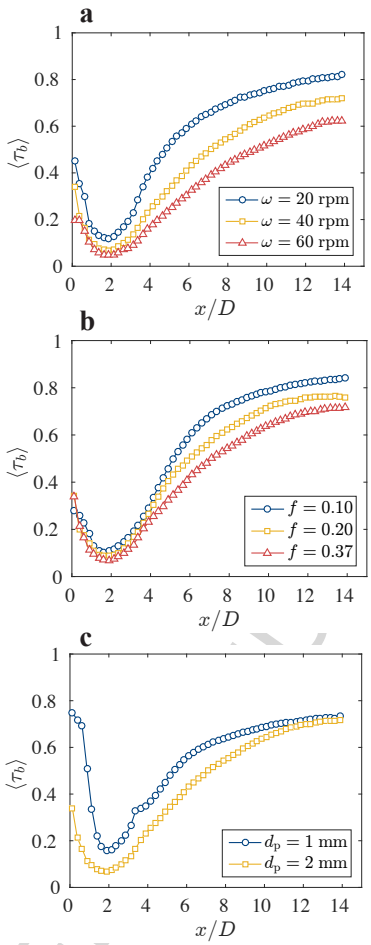

Figure 11: Average temperature profiles of biomass particles in the axial direction. (a) $f = 0.37$ and $d_p = 2$ mm; (b) $\omega = 40$ rpm and $d_p = 2$ mm; (c) $\omega = 40$ rpm and $f = 0.37$.

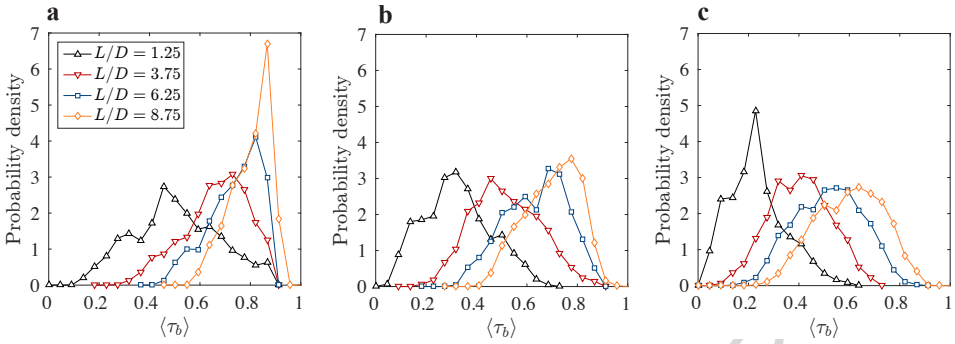

Figure 12: Probability distribution of the biomass particle temperature at screw rotation speed (a) $\omega =$ 20 rpm, (b) $\omega = 40$ rpm and (c) $\omega = 60$ rpm. L/D is the axial distant from the sand feed inlet.

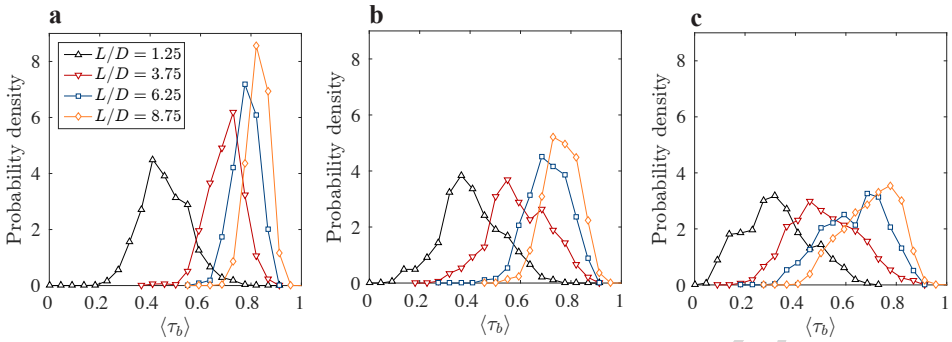

Figure 13: Probability distribution of the biomass particle temperature with volumetric fill level (a) $f = 0.10$, (b) $f = 0.20$ and (c) $f = 0.37$. L/D is the axial distant from the sand feed inlet.

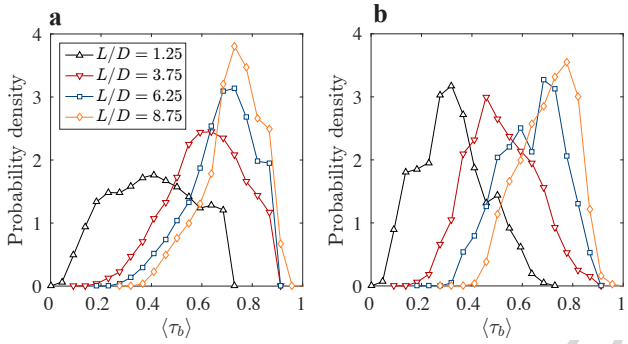

Figure 14: Probability distribution of the biomass particle temperature with particle size (a) $d_p = 1.0$ mm and (b) $d_p = 2.0$ mm. L/D is the axial distant from the sand feed inlet.

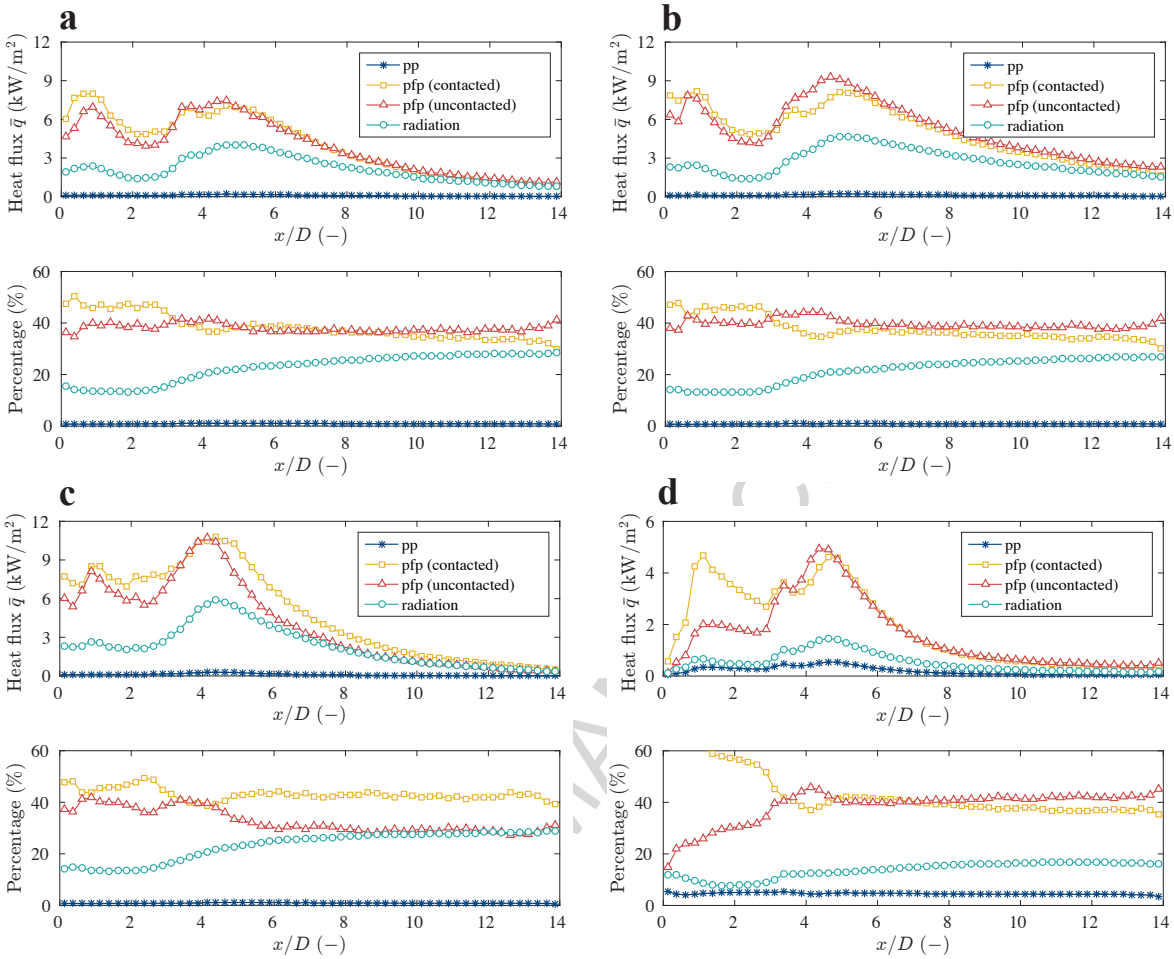

Figure 15: Contribution of different heat transfer pathways. Operating condition: (a) $\omega = 40$ rpm, $f = 0.37$ and $d_p = 2$ mm; (b) $\omega = 60$ rpm, $f = 0.37$ and $d_p = 2$ mm; (c) $\omega = 40$ rpm, $f = 0.10$ and $d_p = 2$ mm; (d) $\omega = 40$ rpm, $f = 0.37$ and $d_p = 1$ mm. *pp* refers to heat conduction through particle-particle contact pathway and *pfp* refers to particle-fluid-particle heat transfer pathway.

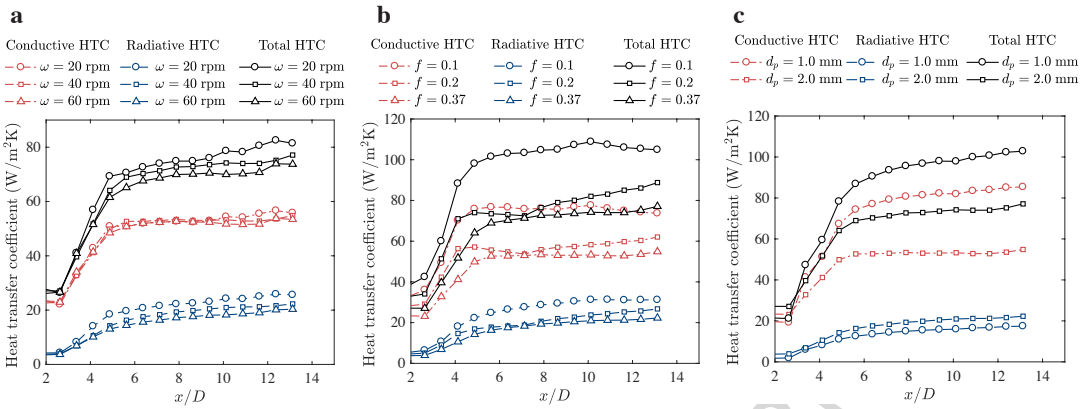

Figure 16: Conductive and radiative heat transfer coefficients in the reactor. Other operation conditions: (a) $f = 0.37$ and $d_p = 2$ mm; (b) $\omega = 40$ rpm and $d_p = 2$ mm; (c) $\omega = 40$ rpm and $f = 0.37$.

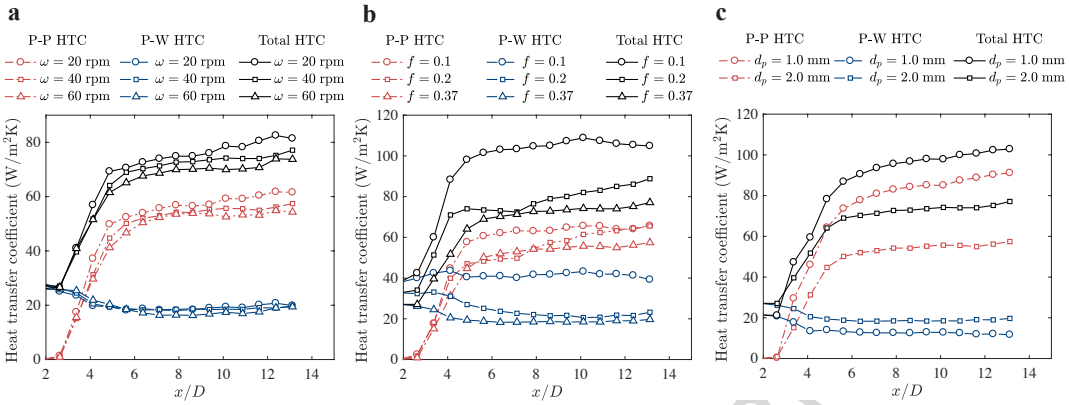

Figure 17: Particle-particle (P-P) and particle-wall (P-W) heat transfer coefficients. Other operation conditions: (a) $f = 0.37$ and $d_p = 2$ mm; (b) $\omega = 40$ rpm and $d_p = 2$ mm; (c) $\omega = 40$ rpm and $f = 0.37$.

Graphical abstract

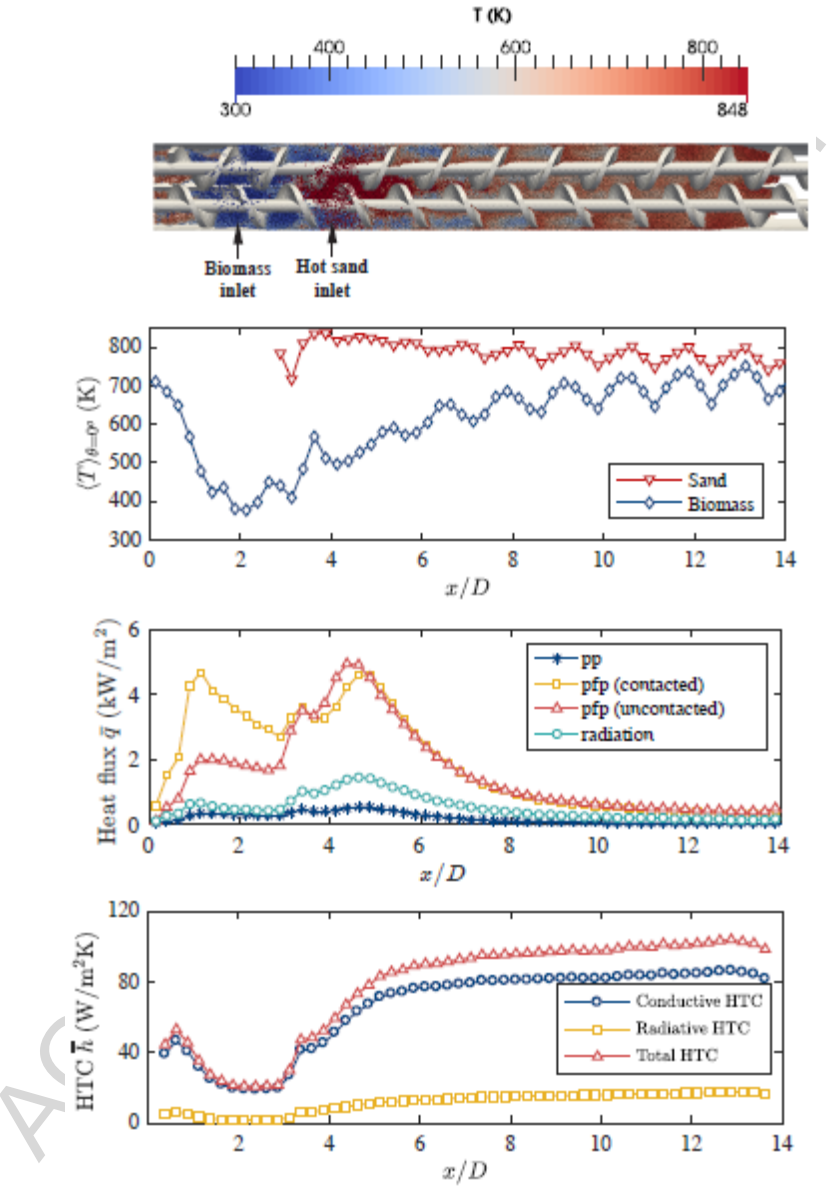

Highlights

- A heat transfer model was developed for modeling heat transfer in granular flows.
- A particle-wall heat transfer model was proposed.
- Particle-fluid-particle is the main contributor to the total heat transfer.
- Radiation contribution to the total heat transfer is significant in the reactor.
- Modeling results indicate a temperature oscillation pattern in the reactor.

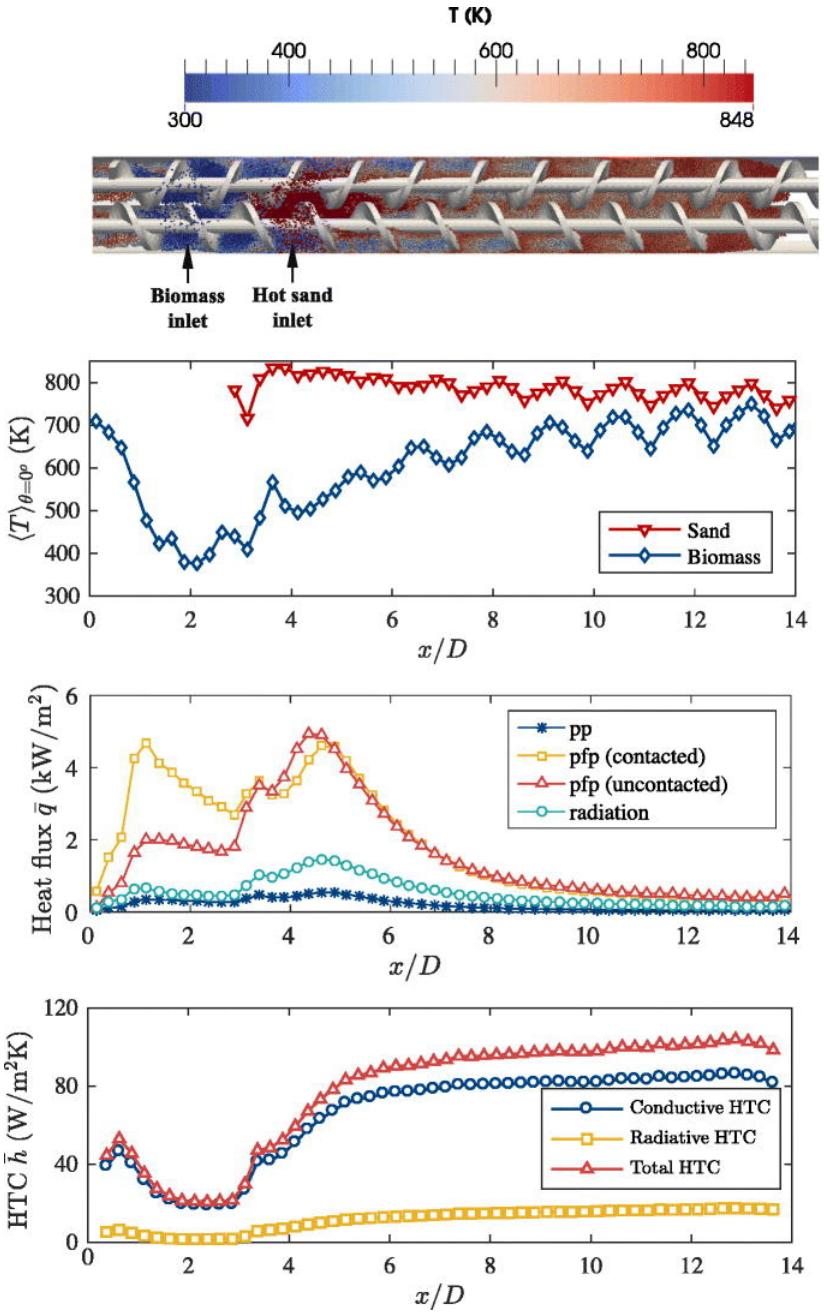

Graphics Abstract

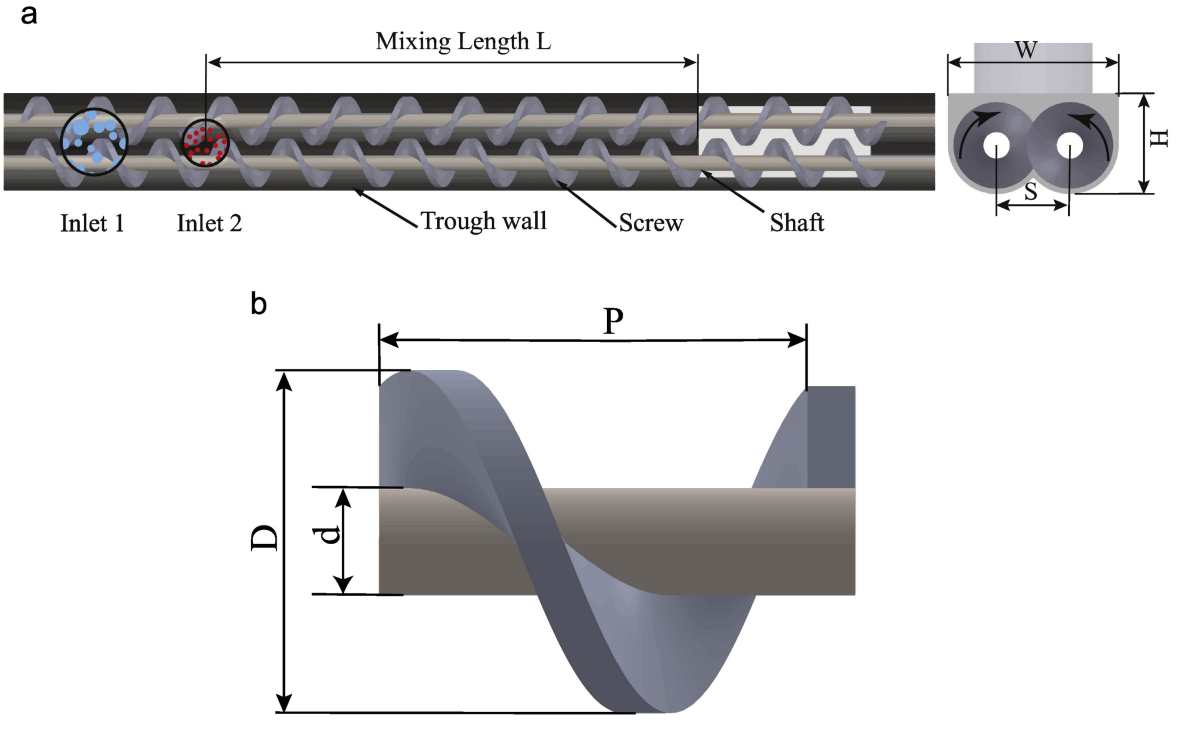
a
Mixing Length L
W
H
S
Inlet 1
Inlet 2
Trough wall
Screw
Shaft
b
P
D
d

Figure 1

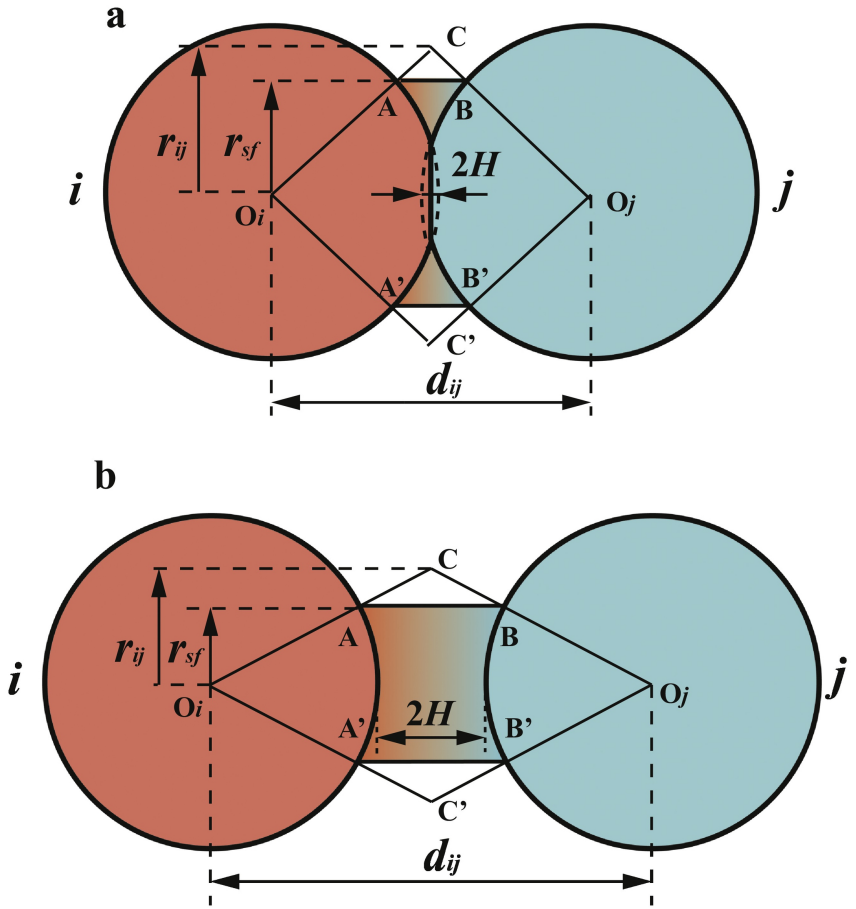

Figure 2

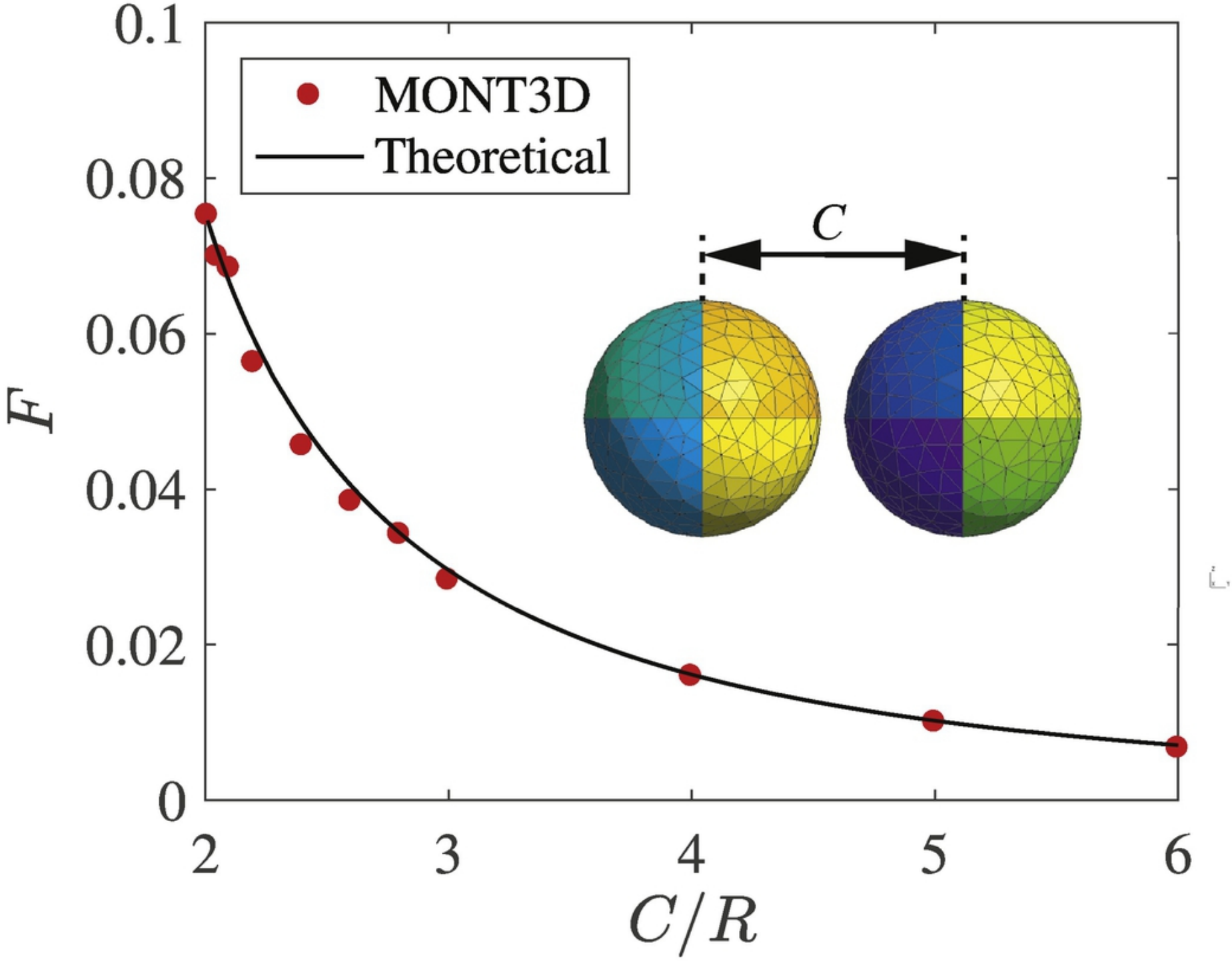

Figure 3

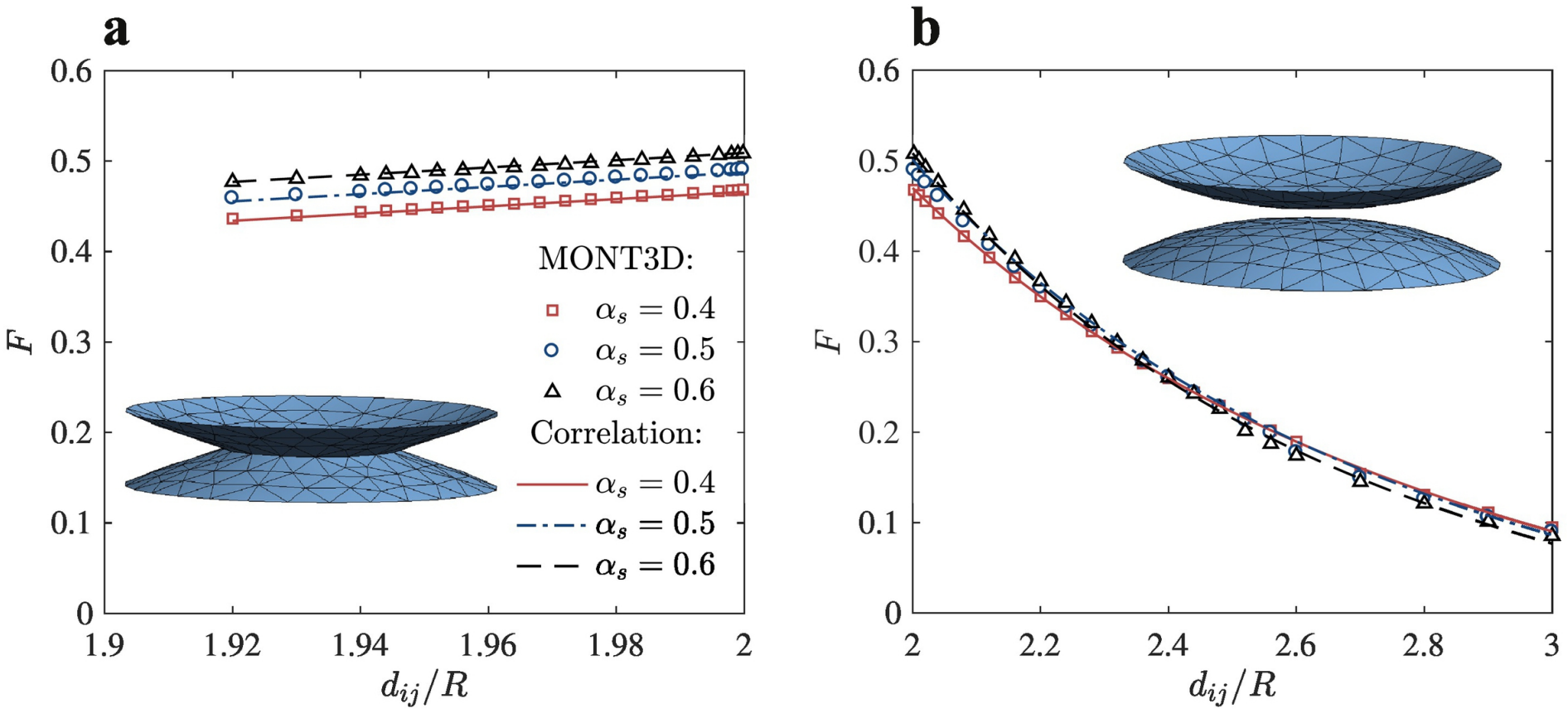
a
b
0.6
0.5
0.4
0.3
0.2
0.1
0
F
1.9
1.92
1.94
1.96
1.98
2
2.2
2.4
2.6
2.8
3
d_{ij}/R
MONT3D:
$\alpha_s = 0.4$
$\alpha_s = 0.5$
$\alpha_s = 0.6$
Correlation:
$\alpha_s = 0.4$
$\alpha_s = 0.5$
$\alpha_s = 0.6$

Figure 4

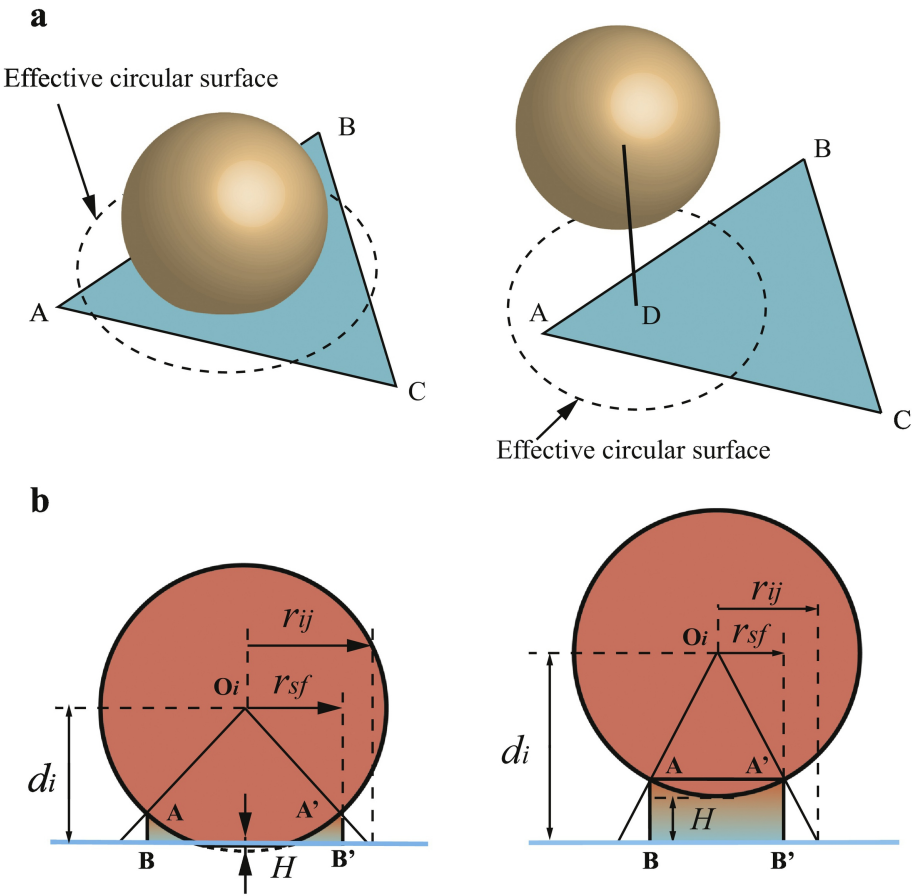
a
Effective circular surface
B
A
C
B
A
D
C
Effective circular surface
b
r_{ij}
Oi
r_{sf}
d_i
A
A'
B
H
B'
r_{ij}
Oi
r_{sf}
d_i
A
A'
H
B
B'

Figure 5

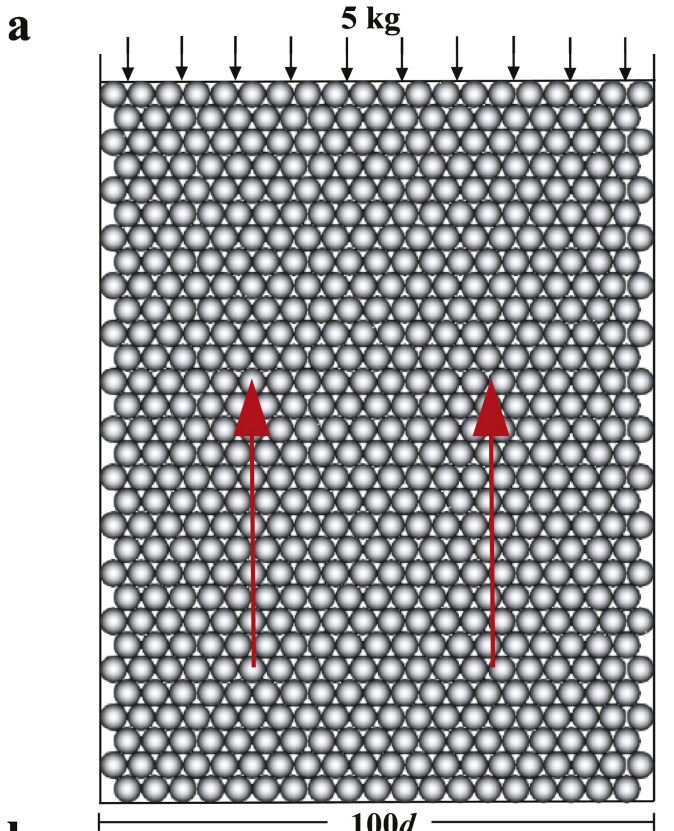
a
5 kg
100d

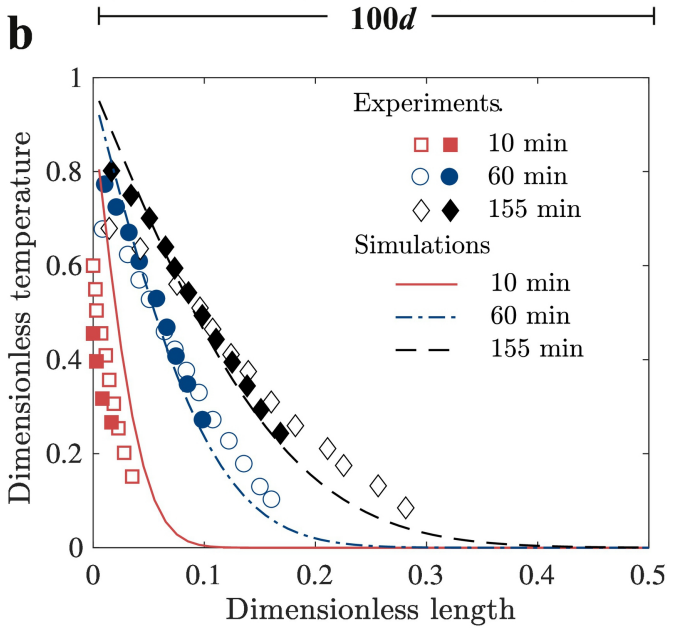
b
Dimensionless temperature
Dimensionless length
Experiments
10 min
60 min
155 min
Simulations
10 min
60 min
155 min
0
0.2
0.4
0.6
0.8
1
0
0.1
0.2
0.3
0.4
0.5

Figure 6

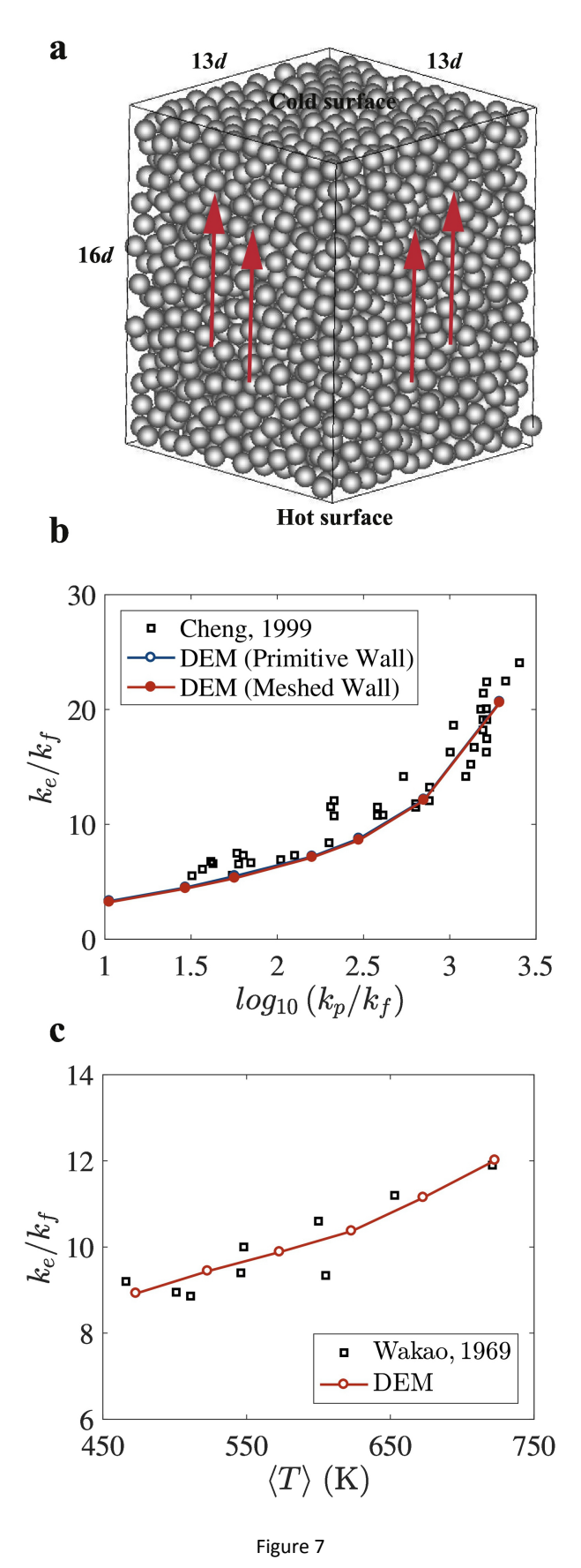
a
13d
13d
Cold surface
16d
Hot surface
b
30
20
10
0
1
1.5
2
2.5
3
3.5
k_e/k_f
$log_{10}(k_p/k_f)$
Cheng, 1999
DEM (Primitive Wall)
DEM (Meshed Wall)
c
14
12
10
8
6
450
550
650
750
k_e/k_f
$\langle T \rangle$ (K)
Wakao, 1969
DEM

Figure 7

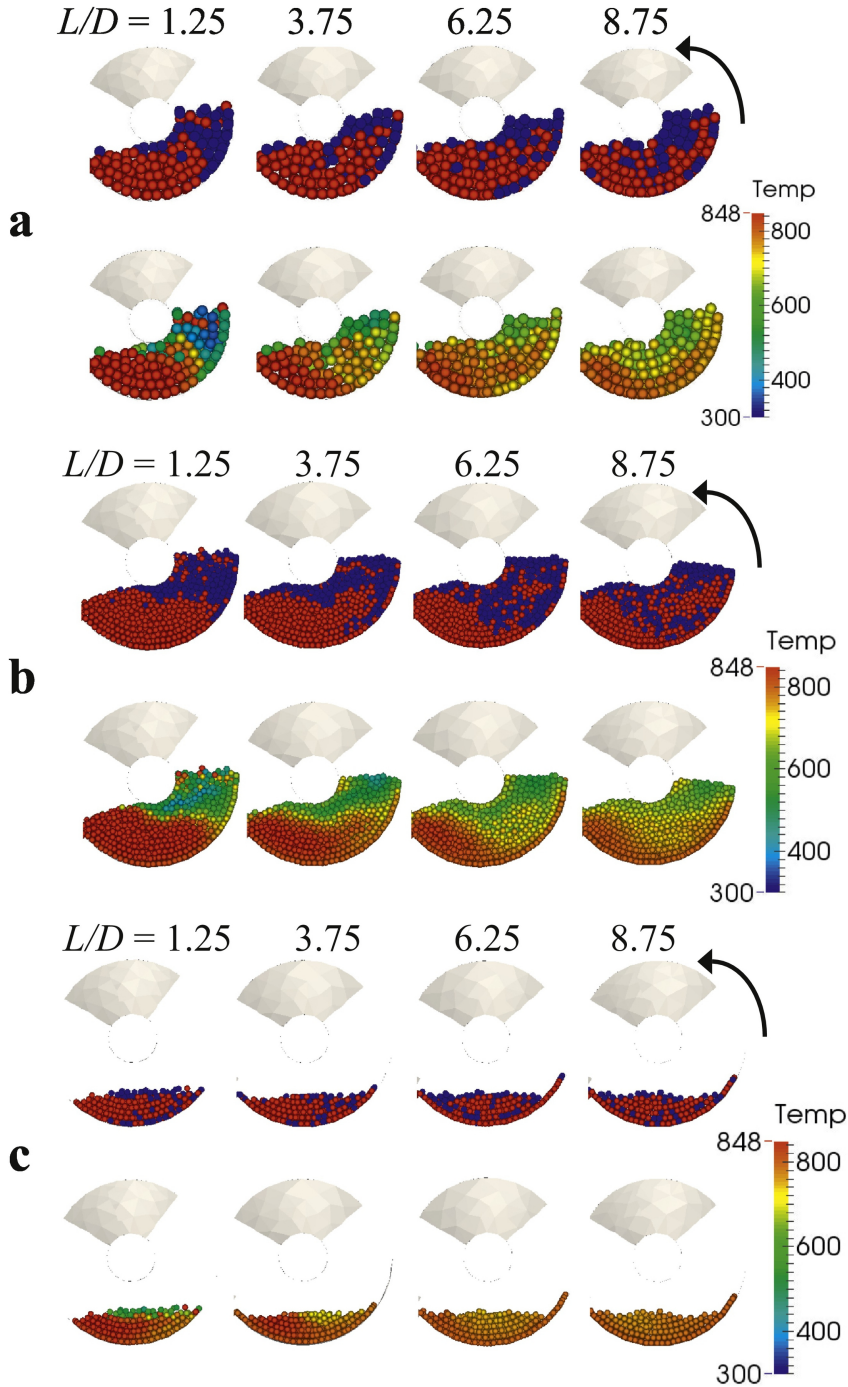
L/D = 1.25
3.75
6.25
8.75
a
Temp
848
800
600
400
300
L/D = 1.25
3.75
6.25
8.75
b
Temp
848
800
600
400
300
L/D = 1.25
3.75
6.25
8.75
c
Temp
848
800
600
400
300

Figure 8

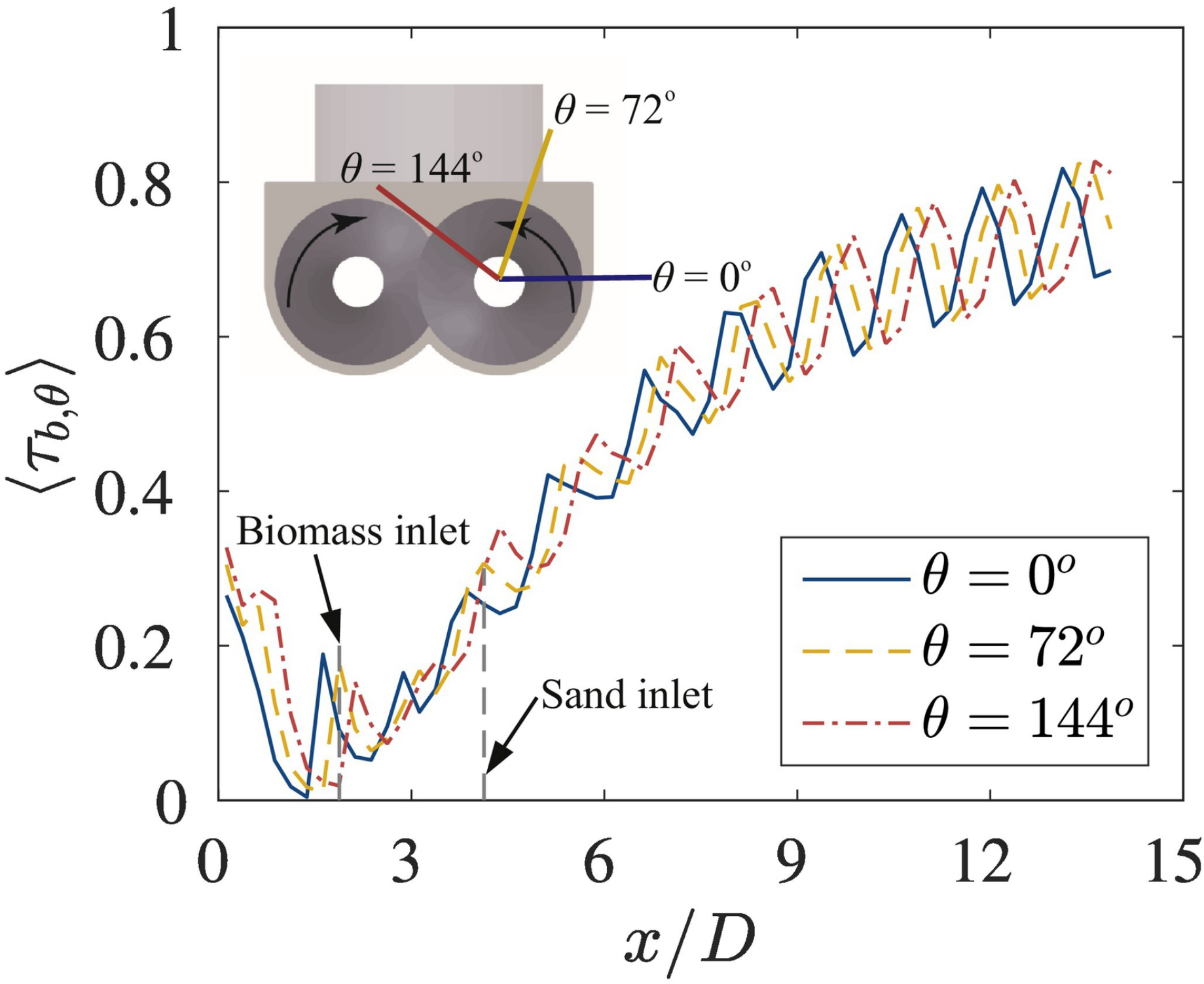
1
0.8
0.6
0.4
0.2
0
$\langle \tau_{b,\theta} \rangle$
$\theta = 72^{o}$
$\theta = 144^{o}$
$\theta = 0^{o}$
Biomass inlet
Sand inlet
$\theta = 0^{o}$
$\theta = 72^{o}$
$\theta = 144^{o}$
0
3
6
9
12
15
x/D

Figure 9

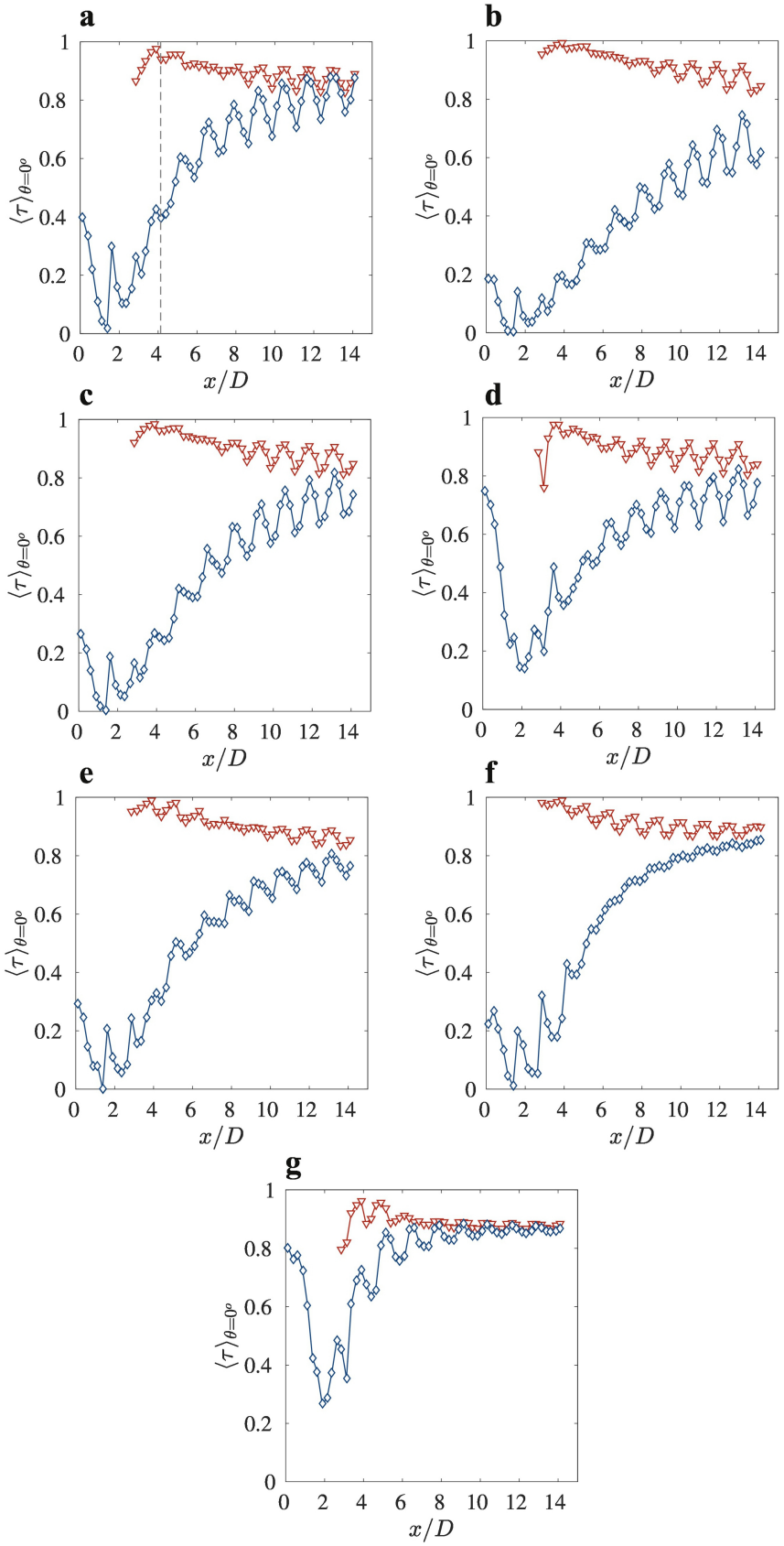
a
b
c
d
e
f
g
$\langle\tau\rangle_{\theta=0^o}$
x/D
0
0.2
0.4
0.6
0.8
1
0
2
4
6
8
10
12
14

Figure 10

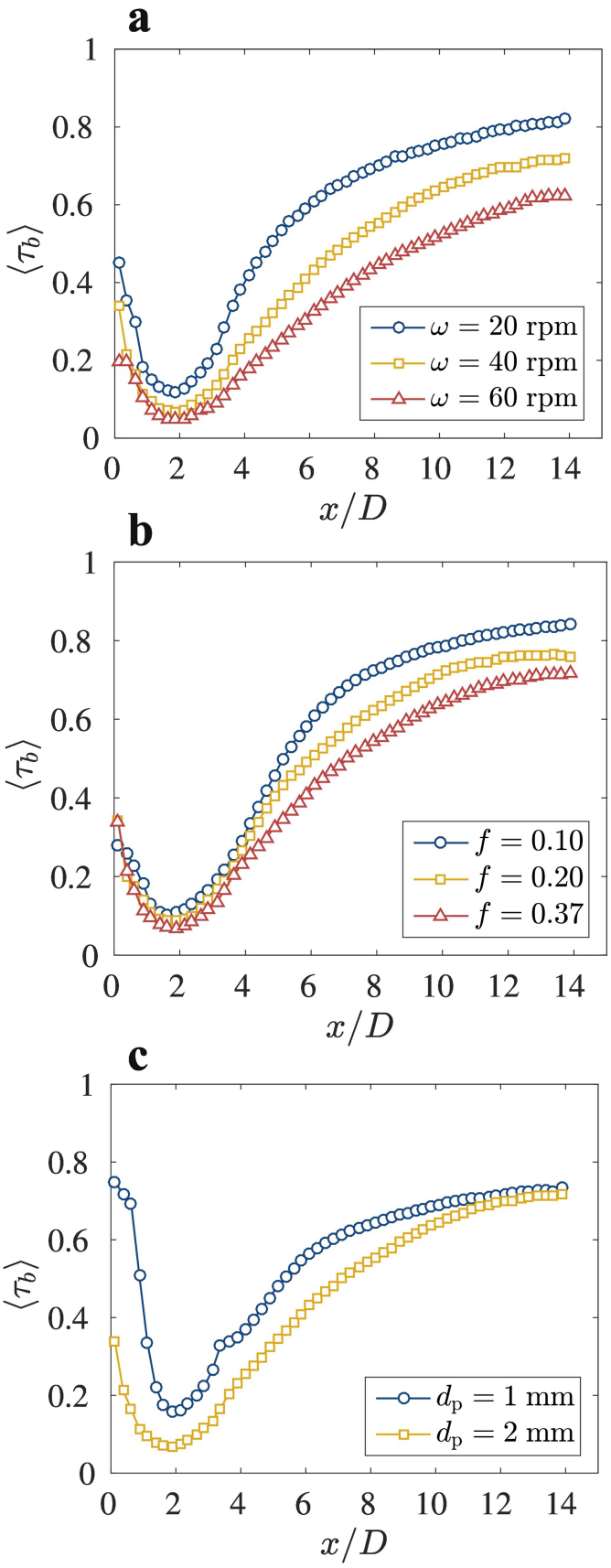
a
1
0.8
0.6
0.4
0.2
0
$\langle \tau_b \rangle$
0
2
4
6
8
10
12
14
x/D
$\omega = 20$ rpm
$\omega = 40$ rpm
$\omega = 60$ rpm
b
1
0.8
0.6
0.4
0.2
0
$\langle \tau_b \rangle$
0
2
4
6
8
10
12
14
x/D
$f = 0.10$
$f = 0.20$
$f = 0.37$
c
1
0.8
0.6
0.4
0.2
0
$\langle \tau_b \rangle$
0
2
4
6
8
10
12
14
x/D
$d_\mathrm{p} = 1$ mm
$d_\mathrm{p} = 2$ mm

Figure 11

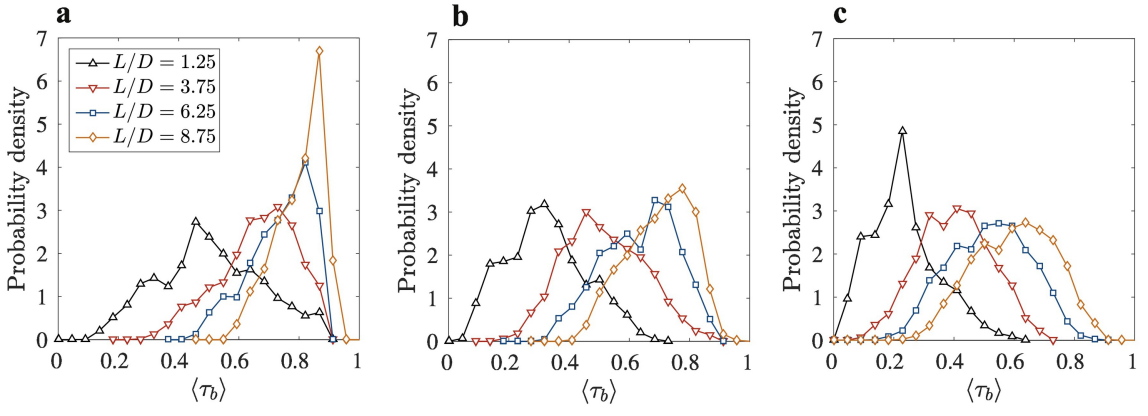
a
b
c
$L/D = 1.25$
$L/D = 3.75$
$L/D = 6.25$
$L/D = 8.75$
Probability density
$\langle \tau_b \rangle$
0
0.2
0.4
0.6
0.8
1
1
2
3
4
5
6
7

Figure 12

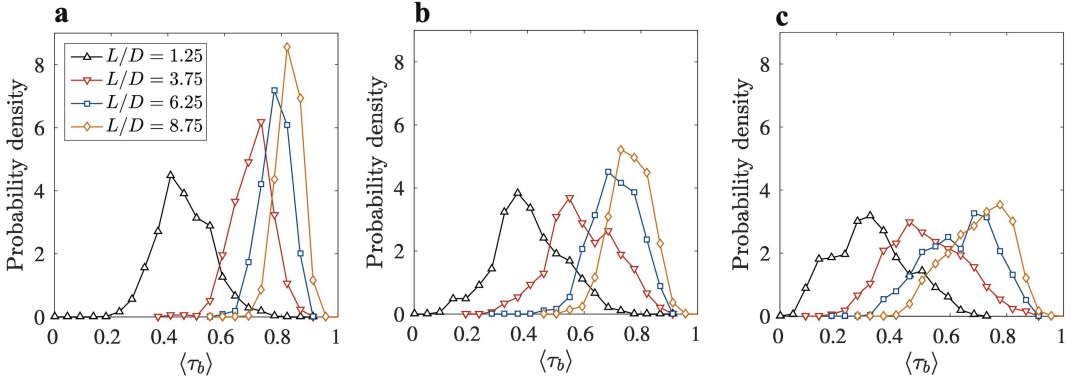
a
b
c
$L/D = 1.25$
$L/D = 3.75$
$L/D = 6.25$
$L/D = 8.75$
Probability density
$\langle \tau_b \rangle$
0
0.2
0.4
0.6
0.8
1
2
4
6
8

Figure 13

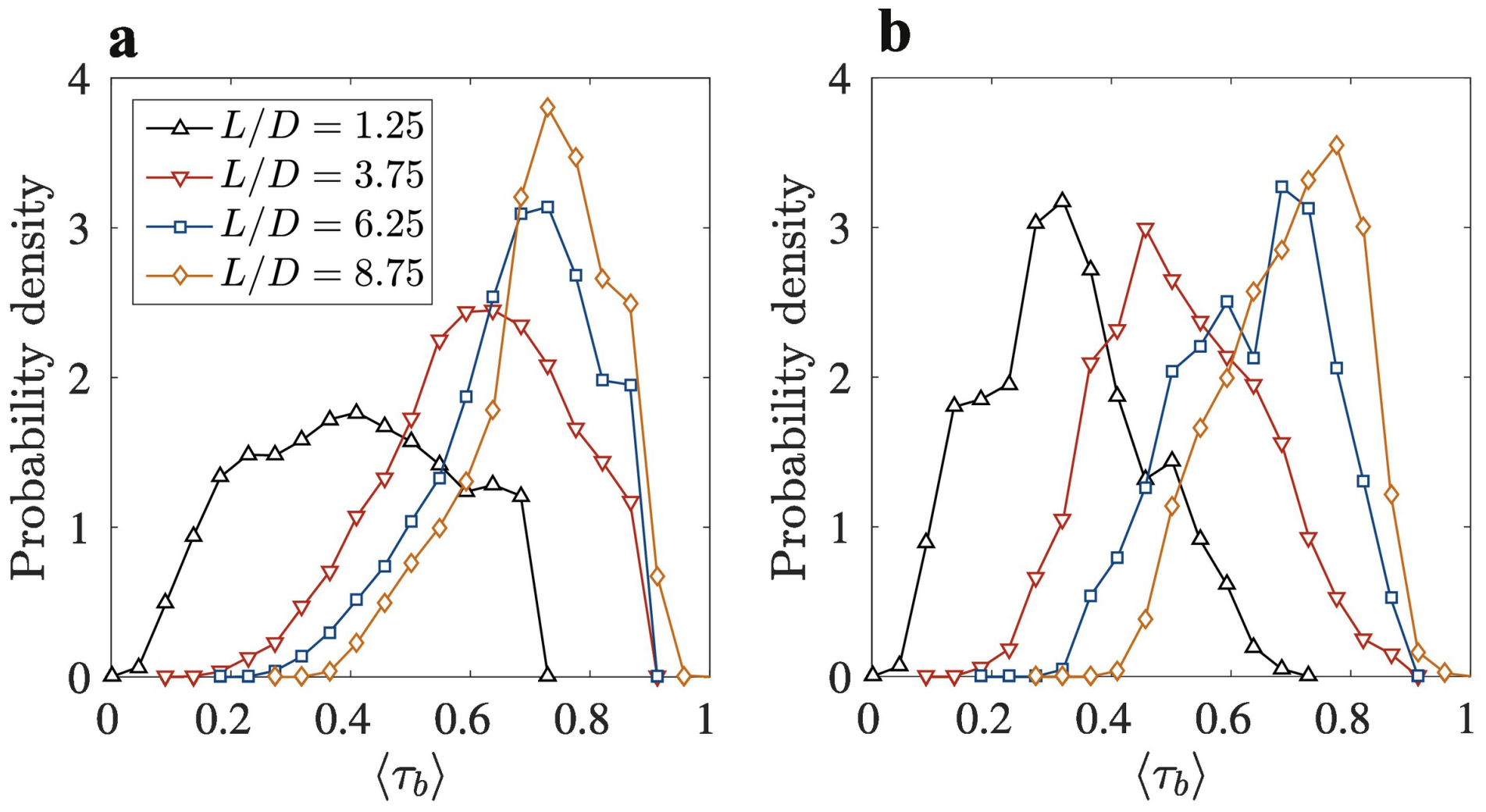
a
b
$L/D = 1.25$
$L/D = 3.75$
$L/D = 6.25$
$L/D = 8.75$
Probability density
$\langle \tau_b \rangle$
0
0.2
0.4
0.6
0.8
1
0
1
2
3
4

Figure 14

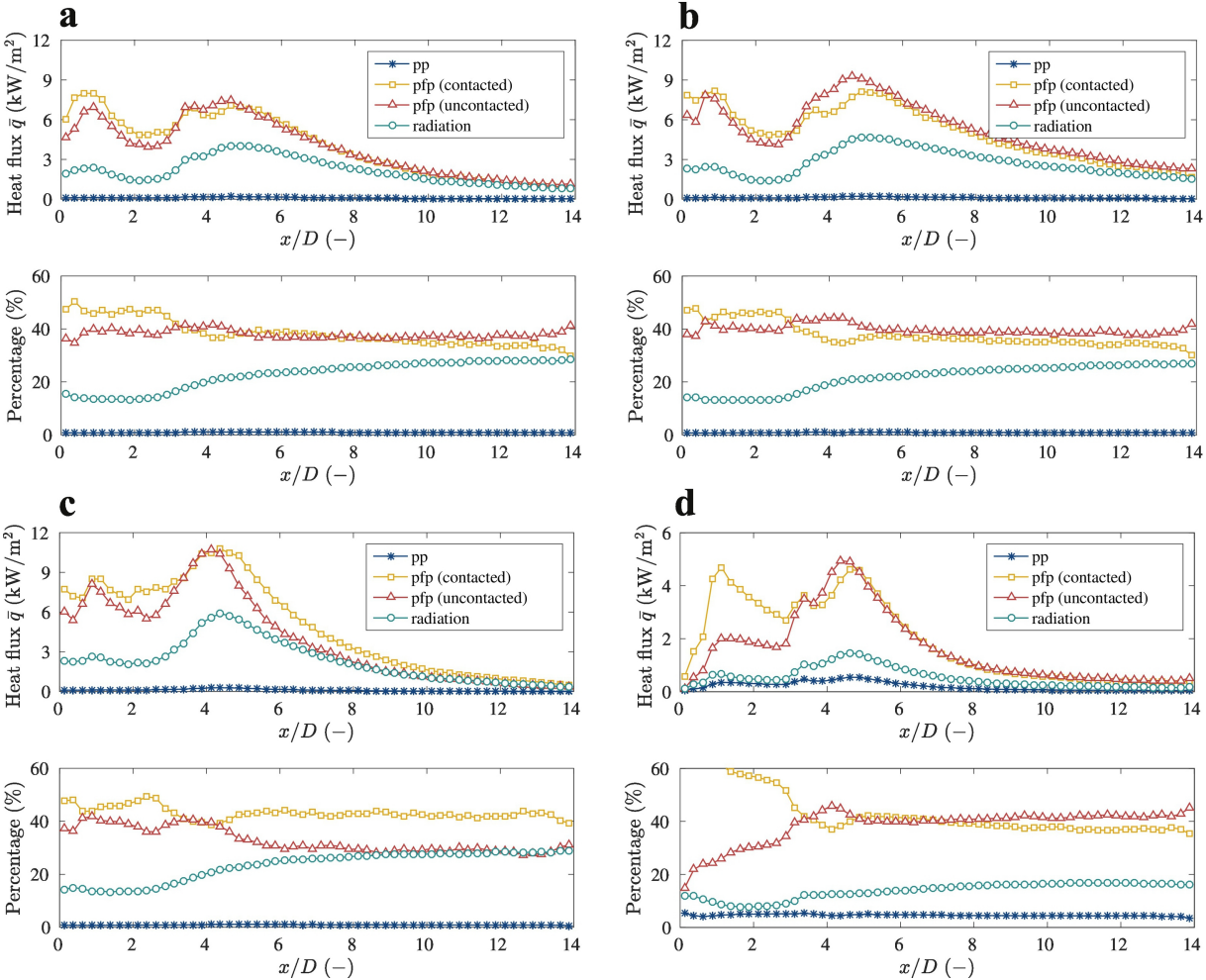
a
b
c
d
Heat flux $\bar{q}$ (kW/m^2)
Percentage (%)
x/D (−)
pp
pfp (contacted)
pfp (uncontacted)
radiation

Figure 15

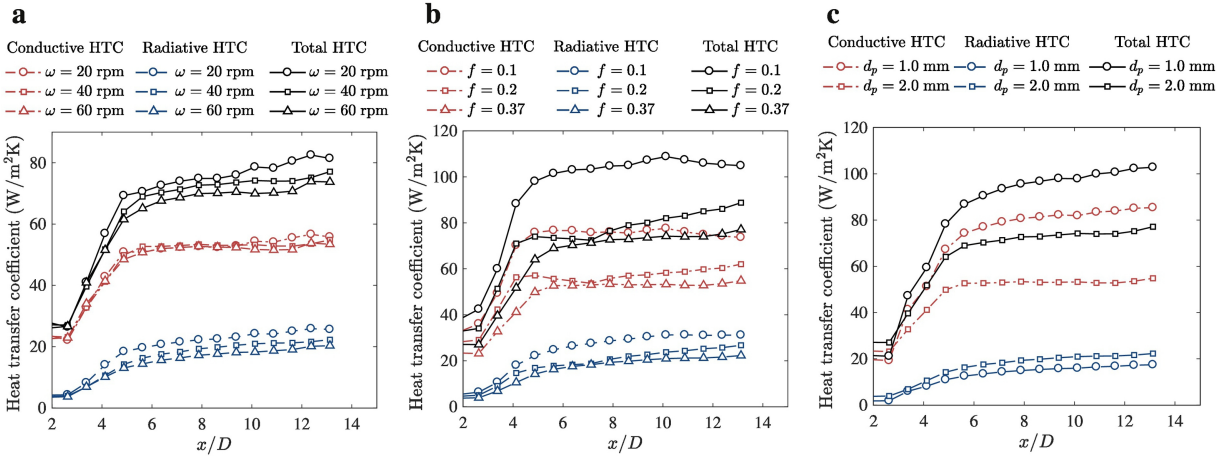
a
Conductive HTC
Radiative HTC
Total HTC
ω = 20 rpm
ω = 40 rpm
ω = 60 rpm
Heat transfer coefficient (W/m²K)
x/D
b
Conductive HTC
Radiative HTC
Total HTC
f = 0.1
f = 0.2
f = 0.37
Heat transfer coefficient (W/m²K)
x/D
c
Conductive HTC
Radiative HTC
Total HTC
d_p = 1.0 mm
d_p = 2.0 mm
Heat transfer coefficient (W/m²K)
x/D

Figure 16

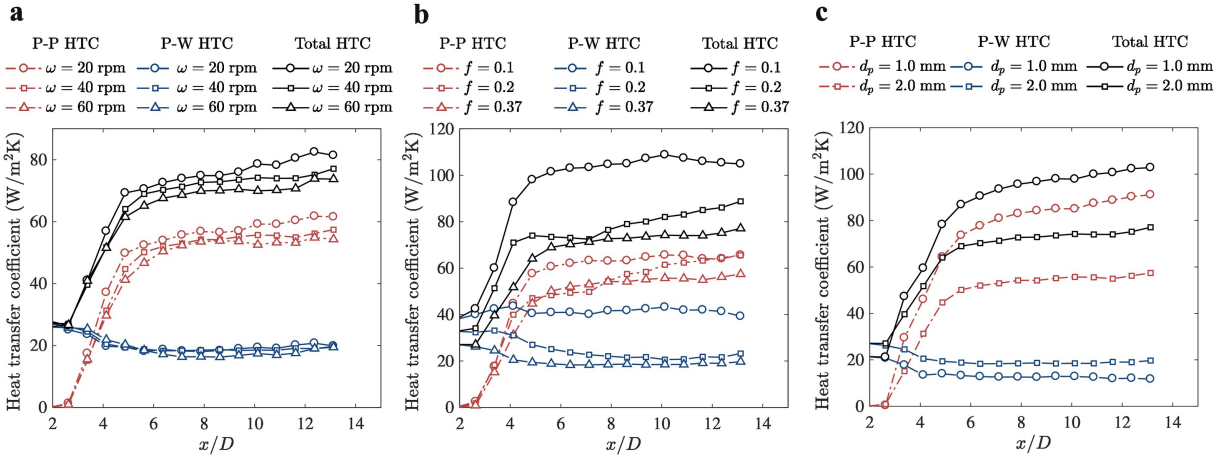
a
P-P HTC
P-W HTC
Total HTC
ω = 20 rpm
ω = 40 rpm
ω = 60 rpm
Heat transfer coefficient (W/m²K)
x/D
b
P-P HTC
P-W HTC
Total HTC
f = 0.1
f = 0.2
f = 0.37
Heat transfer coefficient (W/m²K)
x/D
c
P-P HTC
P-W HTC
Total HTC
d_p = 1.0 mm
d_p = 2.0 mm
Heat transfer coefficient (W/m²K)
x/D

Figure 17